Wayne State University

DigitalCommons@WayneState

Physics and Astronomy Faculty Research Publications

Physics and Astronomy

5-1-2012

The similarity of broad iron lines in X-ray binaries and active galactic nuclei

D. J. Walton
Institute of Astronomy, University of Cambridge

R. C. Reis
Institute of Astronomy, University of Cambridge

E. M. Cackett
Institute of Astronomy, University of Cambridge, ecackett@wayne.edu

A. C. Fabian
Institute of Astronomy, University of Cambridge

J. M. Miller
University of Michigan

The similarity of broad iron lines in X-ray binaries and active galactic nuclei

D. J. Walton,[1]* R. C. Reis,[1,2] E. M. Cackett,[1,3] A. C. Fabian[1] and J. M. Miller[2]

[1]*Institute of Astronomy, Cambridge University, Madingley Road, Cambridge CB3 0HA*
[2]*Department of Astronomy, University of Michigan, 500 Church Street, Ann Arbor, MI 48109, USA*
[3]*Department of Physics and Astronomy, Wayne State University, 666 W Hancock Street, Detroit, MI 48201, USA*

ABSTRACT

We have compared the 2001 *XMM–Newton* spectra of the stellar mass black hole binary XTE J1650−500 and the active galaxy MCG–6-30-15, focusing on the broad, excess emission features at ∼4–7 keV displayed by both sources. Such features are frequently observed in both low-mass X-ray binaries and active galactic nuclei (AGN). For the former case it is generally accepted that the excess arises due to iron emission, but there is some controversy over whether their width is partially enhanced by instrumental processes, and hence also over the intrinsic broadening mechanism. Meanwhile, in the latter case, the origin of this feature is still subject to debate; physically motivated reflection and absorption interpretations are both able to reproduce the observed spectra. In this work we make use of the contemporaneous *BeppoSAX* data to demonstrate that the breadth of the excess observed in XTE J1650−500 is astrophysical rather than instrumental, and proceed to highlight the similarity of the excesses present in this source and MCG–6-30-15. Both optically thick accretion discs and optically thin coronae, which in combination naturally give rise to relativistically broadened iron lines when the disc extends close to the black hole, are commonly observed in both classes of object. The simplest solution is that the broad emission features present arise from a common process, which we argue must be reflection from the inner regions of an accretion disc around a rapidly rotating black hole; for XTE J1650−500 we find spin constraints of $0.84 \leq a^* \leq 0.98$ at the 90 per cent confidence level. Other interpretations proposed for AGN add potentially unnecessary complexities to the theoretical framework of accretion in strong gravity.

Key words: black hole physics – galaxies: active – galaxies: individual: MCG–6-30-15 – X-rays: binaries – X-rays: individual: XTE J1650−500.

1 INTRODUCTION

Simple models for the accretion of material on to a black hole (of any mass) usually include two physically distinct components. The first is an optically thick, geometrically thin accretion disc (Shakura & Sunyaev 1973) formed by material which is gravitationally bound to the black hole, but has sufficient angular momentum to avoid falling directly on to the black hole in the manner discussed by Bondi (1952). The second is a corona of hot electrons, analogous to that seen around the Sun (although the exact geometry and energy distribution of these electrons are not yet well determined; see e.g. Coppi 1999), populated by both thermal and probably non-thermal electrons (Malzac & Belmont 2009). The emission processes relevant to each of these components are relatively well understood. Viscous interactions within the disc heat the material and thermalize

the emission, allowing the disc to be treated as a series of black bodies of increasing temperature with decreasing radius. Some fraction of the thermal emission from the disc is then reprocessed by the coronal electrons, and Compton up-scattered into a power-law-like emission component (Haardt & Maraschi 1991), with a high-energy cut-off determined by the temperature of the thermal electrons, and a low-energy roll-over determined by the temperature of the accretion disc.

The temperature at which the thermal emission from the disc is expected to be observed depends on the mass of the black hole. For the black holes associated with X-ray binaries (XRBs; $M_{BH} \sim 10 \, M_\odot$) the discs are relatively hot and the thermal emission should be observed in the X-ray band at ∼0.2–1.0 keV, while the discs around the much larger black holes associated with active galactic nuclei (AGNs; $M_{BH} \gtrsim 10^6 \, M_\odot$) are much cooler and should be observed in the ultraviolet (UV). However, in both cases the temperature of the coronal electrons is so high (∼100 keV) that the Comptonized emission is always observed in X-rays. Observations

*E-mail: dwalton@ast.cam.ac.uk

of both stellar and supermassive black holes in the UV and X-ray bands have confirmed the presence of these emission components; for XRBs see recent reviews by Remillard & McClintock (2006) and Done, Gierliński & Kubota (2007), and for AGNs see Elvis (2010) and references therein.

With the onset of high-resolution CCD spectroscopy it has become clear that the broad-band X-ray spectra of AGN are in many cases far more complex than the simple power-law continuum expected to be produced by the black hole corona. Additional features arise which can, depending on the intrinsic continuum adopted, be interpreted as originating from either emission or absorption processes, and viable, physically motivated models have been proposed for each case. In emission interpretations the two most prominent features are a broad and smooth excess below $\sim$1.0 keV, commonly referred to as the 'soft excess', and a second broad excess over $\sim$4.0–8.0 keV, while in absorption models these are instead interpreted as a broad absorption trough spanning $\sim$1.0–5.0 keV. The energy of these features, however interpreted, remains remarkably constant, despite the observed AGN hosting black holes spanning many orders of magnitude in mass (see e.g. Gierliński & Done 2004; Crummy et al. 2006; Nandra et al. 2007; Brenneman & Reynolds 2009; Miniutti et al. 2009), which strongly suggests that if they are due to additional emission they must also originate through atomic processes (absorption being an atomic process by nature).

One of the successful emission models is the disc reflection/light bending interpretation which assumes that the corona is compact (or centrally concentrated) and emits some fraction of its flux towards the accretion disc. This is reprocessed into an additional 'reflected' emission component via backscattering, fluorescence and Compton scattering interactions within the surface of the disc (George & Fabian 1991). This reflection component includes discrete atomic features imprinted by the disc, the most prominent of which is usually the neutral iron Kα emission line at 6.4 keV. However, the strong gravity close to a black hole broadens and skews these features via Doppler shifts, beaming and gravitational redshifts (Fabian et al. 1989; Laor 1991). The broad excess over $\sim$4.0–8.0 keV is thus attributed to the iron Kα emission line broadened by such relativistic effects, and the large number of emission lines from iron and lower-mass elements in the $\sim$0.5–1.0 keV range are blended together into a broad and smooth emission component, similar to that observed. The strong gravity also focuses some additional amount of the hard emission down on to the disc through gravitational light bending. This phenomenon causes the spectral variability often observed; if the region in which the Comptonized continuum is produced varies in distance from the central black hole, the fraction of the coronal flux focused on to the disc, and hence that observed, also varies (see e.g. Miniutti & Fabian 2004). For a recent review on X-ray reflection, see Fabian & Ross (2010).

An alternative interpretation is that the observed deviations from the power-law continuum arise as a result of complex absorption due to structures of intervening clouds and infalling/outflowing material. Combinations of these structures can lead to complex combinations of neutral, partially and fully ionized material. Indeed, in a number of AGN there are clear, undeniable signatures of absorption due to partially ionized material (see e.g. Blustin et al. 2005); these 'warm' absorbers are usually associated with mildly outflowing material from the dusty torus or clouds in the broad line region. In addition, there are also detections of absorption by highly ionized material with mildly relativistic blueshifts claimed, which are interpreted as evidence for outflowing disc winds (see Pounds & Reeves 2009; Reeves et al. 2009; Tombesi et al. 2010, and references therein), although it may be necessary to treat a number of these claims

with caution (see Vaughan & Uttley 2008). However, in order to reconcile the large extent of the apparent absorption trough in energy (up to $\sim$5 keV) with its relatively shallow appearance, it is usually necessary to invoke absorption by partially ionized material that only covers some fraction of the X-ray source. With appropriate combinations of these various types of absorption the observed spectra can be reproduced, and spectral variability may be explained via changes in the covering fraction, and/or column density and ionization of the absorbing material. For a review of the absorption processes relevant to AGN, see Turner & Miller (2009).

Even with the quality and quantity of data provided by the latest generation of X-ray observatory, such as *XMM–Newton* and *Chandra*, it has proven very difficult to statistically distinguish between these interpretations for AGN, a case in point being the highly variable AGN MCG–6–30–15 (see Fabian et al. 2002; Miller, Turner & Reeves 2008, who construct statistically acceptable reflection- and absorption-dominated models, respectively). In principle, the simultaneous coverage of the $\sim$0.5–50.0 keV energy range possible with the *Suzaku* satellite may be able to distinguish between disc reflection and pure absorption interpretations in some cases. Reflection models predict the presence of an additional, broad emission feature at $\sim$20–30 keV, referred to as the Compton Hump as it arises due to the interplay of Compton up-scattering of low-energy photons and photoelectric absorption of high-energy photons within the reflecting medium. Features consistent with the Compton Hump are fairly commonly seen in AGN (see e.g. Walton, Reis & Fabian 2010). However, owing to the relatively poor quality data currently available above 10 keV in many cases, these high-energy features can also be consistent with the presence of a partially covering, Compton thick absorber (see e.g. Reeves et al. 2009; Turner et al. 2009).

One of the strongest individual cases in favour of the reflection interpretation is the narrow-line Seyfert 1 galaxy 1H 0707−495, in which reverberation between the power law and reflection components has been detected (see Fabian et al. 2009; Zoghbi et al. 2010). Miller et al. (2010b) argue such apparent reverberation can still be reproduced by distant reflection from the winds required by an absorption-dominated interpretation. However, no absorption model that simultaneously reproduces the reverberation *and* the observed energy spectrum is offered. In addition, it is worth noting that soft excesses are observed in AGN which display no obvious indication of any absorption over that expected due to the Galactic interstellar medium (ISM), e.g. Ark 120 (Vaughan et al. 2004; Nardini et al. 2011) and Ton S180 (Vaughan et al. 2002).

Interestingly, high-quality X-ray spectroscopy of XRBs has also revealed the presence of broad excesses over the Comptonized continuum in the $\sim$4.0–8.0 keV energy range, which are again frequently interpreted as relativistically broadened iron emission lines, e.g. XTE J1650−500 (Miller et al. 2002, Miniutti, Fabian & Miller 2004), GX 339−4 (Reis et al. 2008), GRS 1915+105 (Blum et al. 2009), Swift J1753.5−0127 (Reis et al. 2009a), XTE J1752−223 (Reis et al. 2011). In addition, high-energy features consistent with the Compton Hump are also frequently observed in black hole binaries (BHBs; see e.g. Reis, Fabian & Miller 2010b), supporting the theory that X-ray reflection is present in these sources. Studying XRBs has the advantage that they are often brighter in flux than their AGN counterparts, so the presence of absorption due to outflowing winds, etc., can be tested in greater detail, and their contribution, if any, to the observed spectrum can be determined with much greater confidence.

However, the presence of relativistically broadened iron lines in XRBs is not without its own controversy. Although it is generally accepted that these features do arise due to iron Kα emission, and

that this emission has some finite width, there is some debate over how broad the lines actually are, in particular whether instrumental effects act to artificially enhance the apparent width and skew of the line profile, and therefore over the mechanism that broadens them. This is entwined with the debate over whether the accretion disc extends in to the inner-most stable circular orbit (ISCO). While it is generally accepted that this is the case at high accretion rates, and that at some low accretion rate the optically thick disc most likely begins to truncate at a larger radius within which a hot, advection-dominated accretion flow arises, the accretion rate at which truncation occurs is still under dispute. Some authors, e.g. Done et al. (2007), argue that the disc begins to truncate during the transition between the high/soft and low/hard accretion states, while others, e.g. Reis et al. (2010b), argue that the disc remains at the ISCO until much lower accretion rates (for a review of the 'standard' accretion states displayed by BHBs, see Remillard & McClintock 2006).

If, as is likely, the line is produced in the disc, then as the disc recedes the line profile should evolve and become narrower. However, BHBs in the low/hard state still appear to display similarly broad excesses to other accretion states (see e.g. Reis et al. 2011). Liu, Done & Taam (2011) proposed a modification to the truncated disc model, in which the outer disc truncates, but some inner portion remains, resulting in a disc with a hole in it. Such a geometry would allow the truncated disc model and the broad iron line observations to be reconciled without invoking a separate medium that produces the line. However, through analysis of the variability displayed by both the thermal and Comptonized components of GX 339−4 in the low/hard state, Wilkinson & Uttley (2009) show that in order for the variability to be driven by fluctuations in the mass accretion rate, as is generally thought to be the case, the disc must extend uninterrupted to at least $20R_\mathrm{G}$, placing strict constraints on the location and size of any hole which render this scenario unlikely. The truncated disc interpretation therefore requires that the dominant line broadening mechanism is some process other than Doppler/gravitational effects, as this interpretation frequently requires that the disc extends close to the black hole.

An alternative mechanism that has been invoked to explain broad line profiles is Compton broadening, in which Compton scattering of line photons modifies their energy (see e.g. Czerny, Zbyszewska & Raine 1991; Misra & Sutaria 1999; Di Salvo et al. 2005; Titarchuk, Laurent & Shaposhnikov 2009). This process broadens and, depending on the conditions of the Comptonizing region, can even skew the line profile. Some contribution from Compton broadening is unavoidable for any realistic method of line production, as the line emission will necessarily be Compton scattered as it escapes from the medium in which it is produced. If the line is associated with the disc, Compton broadening is expected to be a more significant process for BHBs than for their AGN counterparts owing to their relative disc temperatures (Ross & Fabian 2007). The challenge then becomes determining the relative contribution to the line profile of this process and the relativistic effects discussed above. However, it has also been proposed that the line does not originate in the disc, but is instead produced via recombination in the corona or in a disc wind. These scenarios require Compton broadening to play a prominent role in determining the line profile. We note that given the changes in the corona and the changes in mass inflow and outflow rate typically observed during the evolution of BHB outbursts, evolution in the line profile would also be expected for these latter scenarios.

Here, we present an analysis of the high-quality X-ray spectra of the XRB XTE J1650−500, which displays a broad line profile.

Both relativistic and Compton broadening are examined, and we demonstrate that the former scenario is strongly preferred. We then proceed to compare the high-energy spectra of XTE J1650−500 and the AGN MCG–6-30-15, and demonstrate the similarity of the features identified as broad iron lines in each case. This work is structured as follows: Section 2 gives details on the data reduction; Section 3 presents our spectral analysis, highlighting the similarity of the two line profiles and finally Section 4 presents our discussion, in which we use this comparison as the basis for a simple, logical argument in favour of the reflection interpretation for AGN.

2 OBSERVATIONS AND DATA REDUCTION

XTE J1650−500 and MCG–6-30-15 were both observed with *XMM–Newton* (Jansen et al. 2001) in 2001 September and August, respectively. In addition, XTE J1650−500 was observed three times by *BeppoSAX* (Boella et al. 1997a) during the same outburst. The first *BeppoSAX* and the *XMM–Newton* observations of XTE J1650−500, separated by about a day, caught the source in a rising intermediate state, i.e. during the transition between the low/hard and high/soft states in which the thermal and Comptonized emission components are both strong. The latter two *BeppoSAX* observations, taken further along the evolution of the outburst, found the source in a more traditional high/soft state. These observations were selected because they represent some of the best quality X-ray data available for XRBs and AGNs, as the data obtained have good photon statistics, the *XMM–Newton* observation provides low-energy coverage and the *BeppoSAX* data provide a view of the emission from XTE J1650−500 at ∼6 keV with an independent detector. Here we detail the data reduction procedure adopted for each source. In both cases the *XMM–Newton* reduction was carried out with the *XMM–Newton* Science Analysis System (SAS version 10.0.0).

2.1 XTE J1650−500

The 2001 observation of XTE J1650−500 was taken on September 13 with the *EPIC*-pn (Strüder et al. 2001) CCD in burst mode, so despite its extremely high flux, the spectrum obtained with this detector is not expected to suffer from pile-up.[1] The data reduction procedure adopted for this source follows closely that outlined in Kirsch et al. (2006). The *EPIC*-pn observation data files were processed using EPCHAIN to produce calibrated event lists from which spectral and timing products may be extracted. Burst mode is similar to timing mode and operates with extremely fast readout times; 200 lines of CCD pixels are fast-shifted in 14.4 μs as the source data are being recorded. This readout process leads to the loss of spatial information in the shift (RAWY/CCD line number) direction; such information is only available in the direction on the CCD perpendicular to the readout (RAWX/CCD column number). Despite the extremely fast readout employed in burst mode, Kirsch et al. (2006) found that events with RAWY > 140 contain piled-up data, so we extracted the source spectrum from the region bounded by 0 ≤ RAWY ≤ 140 and 27 ≤ RAWX ≤ 46. In addition, we also only included single and double events, and excluded border pixel events. As XTE J1650−500 was so bright during this observation, there was no region on the operational CCD free of source counts,

---

[1] Pile-up refers to the situation in which more than one photon is incident on a CCD pixel within a single readout time. These are incorrectly registered as a single photon at an artificially high energy. For a detailed description of this effect, see Miller et al. (2010a) and references therein.

so we did not extract a background spectrum following the recommendation of the *XMM–Newton* burst mode reduction guide.[2] Given the high source count rate (see below), the contribution of background counts should be negligible. The redistribution matrices and auxiliary response files were generated with RMFGEN and ARFGEN, respectively. The spectrum obtained had a good exposure time of 685 s, and an average total count rate of 2504 ± 2 count s^{-1}. Finally, the spectrum was grouped using GRPPHA such that each energy bin contained a minimum of 25 counts, so that the probability distribution of counts within each bin can be considered Gaussian, and hence the use of the χ^2 statistic is appropriate when performing spectral fits. The *EPIC*-MOS detectors were not operated for this observation, and we do not consider the spectrum obtained with the RGS instrument in this work, as it suffers quite severely from pile-up effects.

Throughout this work, we also make use of the three *BeppoSAX* observations taken during the course of the same outburst. These were obtained on 2001 September 11, 21 and October 3, respectively. We reduced the MECS (Boella et al. 1997b) data for each observation following the prescription outlined in the *BeppoSAX* cookbook.[3] In each case we defined a circular source region of radius 8 arcmin, and a circular background region free of other sources of the same size, and use the appropriate 1997 September auxiliary response and redistribution files. The good exposure times and average count rates obtained for each observation are 47, 68 and 24 ks and 34.18 ± 0.03, 42.18 ± 0.03 and 32.57 ± 0.03 count s^{-1}, respectively. Note that the MECS detector has a lower energy resolution than *EPIC*-pn ($\sim$750 eV in comparison to $\sim$150 eV at 6 keV).

2.2 MCG–6-30-15

The long 2001 observation of MCG–6-30-15 was taken in small window mode, and spanned three orbits. Data reduction was carried out separately for each orbit, largely according to the standard prescription provided in the online guide.[4] In this work we focus on the *EPIC*-pn data for direct comparison with XTE J1650−500. The observation data files were processed using EPCHAIN to produce calibrated event lists. Spectra were produced for the 0.5–10.0 keV energy range selecting only single and double events using XMM-SELECT, and periods of high background were treated according to the method outlined by Piconcelli et al. (2004), with the signal-to-noise ratio maximized for the 6.0–10.0 keV energy band, where the neutral and ionized iron transitions are expected to be observed. A circular source region of radius 37 arcsec was defined in order to include as many source counts as possible without including CCD chip edges, and a larger circular background region of radius 54 arcsec was chosen in an area of the same CCD free of other sources. The redistribution matrices and auxiliary response files were generated with RMFGEN and ARFGEN. After performing the data reduction separately for each of the orbits, the spectra were combined using the FTOOL[5] ADDSPEC, which combines spectra in a response weighted manner to account for any differences there may be in, e.g., the exposure times, etc. ADDSPEC also automatically combines the instrumental responses and background spectra associated with the source spectra. The resulting spectrum had a good exposure time of 221 ks, and an average total count rate of

28.15 ± 0.01 count s^{-1}. Finally, for the same reason as for XTE J1650−500, the spectrum was grouped using GRPPHA to have a minimum of 25 counts in each energy bin.

3 SPECTRAL ANALYSIS

Here we detail our spectral analysis of XTE J1650−500 and MCG–6-30-15. The approach for XTE J1650−500 is simple: we begin by modelling the continuum to highlight the broad line profile, before modelling the line in a phenomenological fashion and finally moving on to a more physical treatment of the disc reflection. In addition, we also consider Compton broadening in some detail and find that strong relativistic effects are still required to explain the breadth of the line. We then construct a simple phenomenological model for the spectrum of MCG–6-30-15 in order to again highlight the line profile in this source, and its similarity to that of XTE J1650−500 (a full physical interpretation of MCG–6-30-15 is presented in Chiang & Fabian 2011, utilizing all currently available data, and so will not be undertaken here.). Spectral analysis is performed with XSPEC v12.6.0f (Arnaud 1996), and quoted uncertainties on model parameters are the 90 per cent confidence limits for one parameter of interest determined by χ^2 variation, unless stated otherwise. In both cases, due to calibration uncertainties possibly related to a deficient charge transfer inefficiency (CTI) correction at high count rates (see Section 3.1.7 for a description of the effects of CTI), significant negative residuals were continually observed associated with the instrumental silicon K and gold M edges at $\sim$1.8 and 2.2 keV, respectively, hence the energy range 1.7–2.5 keV has been excluded from our analysis throughout this work. We adopt the solar abundances given in Wilms, Allen & McCray (2000).

3.1 XTE J1650−500

3.1.1 Continuum modelling

We model the continuum of XTE J1650−500 with the standard BHB components, namely a multi-colour blackbody accretion disc (modelled with DISKBB; Mitsuda et al. 1984) which accounts for the thermal emission from the disc and dominates at soft energies, and a power law, associated with Comptonization of the thermal emission by electrons in a corona, which dominates at hard energies. Both of these are modified by Galactic absorption, accounted for with the TBABS absorption code (Wilms et al. 2000). The column density of the ISM, as well as its oxygen, neon and iron abundances, was allowed to vary; all other elements were assumed to have solar abundances. The 4.0–8.0 keV data were not considered at this stage of the analysis, in order to minimize any contribution from the iron emission region to our determination of the continuum. This model was fit to the remaining data, and although statistically it is not formally acceptable, with $\chi^2_\nu = 1184/865$, it provides a good representation of the general shape of the spectrum. The relatively poor fit statistic is mostly due to residual features at $\sim$0.6–0.8 keV (see Fig. 1), which will be discussed in Section 3.1.5; the data closer to the 4.0–8.0 keV range, where the iron line is expected to be observed, are well modelled.
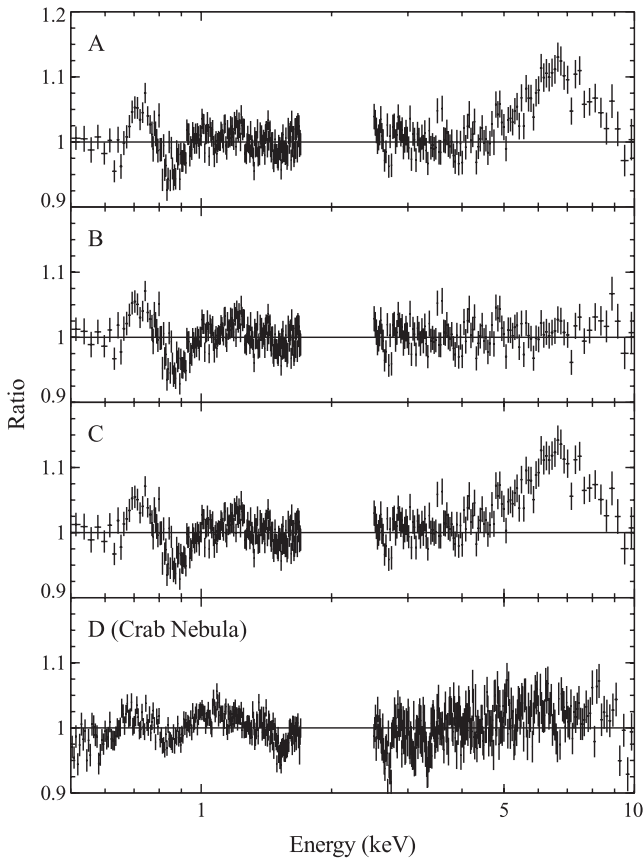
3.1.2 Line profile

We now include the 4.0–8.0 keV data in our analysis. Fig. 1 (panel A) shows the data/model ratio of the full 0.5–10.0 keV spectrum for XTE J1650−500 to the previously determined continuum model. It is clear that there is a large, broad excess in the ratio

---

Figure 1. Data/model ratio plots for XTE J1650−500. Panel A: ratio plot to the continuum model fit to the 0.5–4.0 and 8.0–10.0 keV data (see Section 3.1.1); the broad iron line profile is clearly shown. Panel B: the ratio plot when a LAOR2 line is included in the model; the iron line is clearly well modelled. Panel C: ratio plot to the model including the LAOR2 line with the line normalization set to zero to demonstrate that this component accounts for the hard residuals without drastically altering the continuum. Soft residual features over the ∼0.6–0.8 keV energy range are seen throughout; these are discussed in Sections 3.1.4 and 3.1.6. Panel D: ratio plot of the 2002 burst mode spectrum of the Crab nebula modelled with an absorbed power law (see Section 3.1.4). Similar soft residuals are seen, implying these features possibly arise due to systematic uncertainties. The spectra have been rebinned for clarity.

spectrum in this energy range, which we interpret as arising due to iron emission. Initially, we modelled the line profile with a Gaussian emission line component, with the rest-frame energy of the line constrained to be between the neutral iron Kα transition at 6.4 keV and the iron Ly α transition at 6.97 keV, as the discs in XRBs are likely to be highly ionized (Ross & Fabian 2007). With the inclusion of the Gaussian line the model provides a fairly good fit to the data, with

$\chi^2_\nu = 1936/1663$. The soft residuals highlighted previously are still present, but the line profile is well modelled. We find that the line energy is constrained to the lower end of the allowed energy range in contrast with the expectation for an ionized disc, with $E_{Gauss} < 6.5$ keV, and the profile is very broad, with $\sigma = 1.17^{+0.24}_{-0.21}$ keV. The equivalent width (EW) obtained is EW $= 350^{+130}_{-110}$ eV.

If the iron line is primarily broadened by gravitational and Doppler effects, then its width implies the disc must extend to the regions of strong gravity close to the black hole. We replaced the Gaussian emission line with a LAOR2 line (Laor 1991), which applies the relevant relativistic effects to a Gaussian emission line profile. The parameters of this component are the energy of the emission line, the inner and outer radii of the accretion disc in gravitational radii ($R_G = GM/c^2$), the inclination of the disc, i, the indices of the radial emissivity profile, assumed to be a broken power law of form:

$$\epsilon(r) \propto \begin{cases} r^{-q_{inner}} & r < R_{br} \\ r^{-q_{outer}} & r > R_{br} \end{cases} \qquad (1)$$

and the break radius of the emissivity profile, also in gravitational radii. Recent simulations have suggested the radial emissivity profile may indeed be more complex than a single power law, showing a break at ∼6 R_G (Miniutti & Fabian 2004; Wilkins & Fabian 2011). The outer radius of the disc was taken as the maximum allowed by the model, 400 R_G (this parameter is rarely well constrained as even in the case of a Schwarzschild black hole the majority of the emission arises from the innermost regions of the disc.). The rest of the line parameters were initially free to vary, although in the course of the modelling we found that R_{br} and q_{outer} could not be constrained. These were, respectively, set to $R_{br} = 6R_G$, after which the metric tends asymptotically towards the Schwarzschild case even for a maximally rotating Kerr black hole, and $q_{outer} = 3$, as expected for a lamp-post illumination model. With the inclusion of the LAOR2 line, the model again provides a fairly good fit to the data, with $\chi^2_\nu = 1936/1661$. The parameters and EW obtained for the LAOR2 profile are given in Table 1 and the data/model ratio plot is shown in Fig. 1 (panel B). The energy of 6.97 keV obtained for the iron line with this profile is more consistent with the expectation of a highly ionized disc. In Fig. 1 (panel C) we also show the ratio plot for the model including the LAOR2 line, but with the line normalization set to zero, to demonstrate that this component models the hard residuals well without significantly altering the continuum model determined previously.

3.1.3 High-energy Comptonization

Although the high-energy Comptonized continuum is often power-law like in the *XMM–Newton* bandpass, we also investigated whether this approximation has any effect on the line profile. To test this, we also modelled the high-energy continuum with the

Table 1. Key continuum and iron line parameters obtained by phenomenologically modelling the broad line profiles of XTE J1650−500 and MCG–6-30-15 with LAOR line models. Parameters marked with * have not been allowed to vary, and those with 'p' quoted as one of the limits have reached the relevant constraint imposed upon it. The rest-frame energies of the iron emission lines were required to be in the range 6.40–6.97 keV. The temperatures quoted are of the DISKBB component for XTE J1650−500, and of the blackbody included to account for the soft excess in MCG–6-30-15.

	Γ	T (keV)	E (keV)	R_{in} (R_G)	R_{br} (R_G)	R_{out} (R_G)	q_{inner}	q_{outer}	i (°)	EW (eV)
XTE J1650−500	$2.14^{+0.02}_{-0.01}$	0.295 ± 0.007	$6.97^p_{-0.30}$	$1.47^{+0.08}_{-0.03}$	6*	400*	>8.2	3*	69^{+3}_{-8}	370^{+100}_{-70}
MCG–6-30-15	1.961 ± 0.004	0.123 ± 0.002	$6.40^{+0.04}_p$	$1.9^{+0.2}_{-0.1}$	8^{+28}_{-3}	400*	$4.8^{+1.6}_{-0.9}$	2.2 ± 0.3	47^{+4}_{-2}	430^{+120}_{-70}
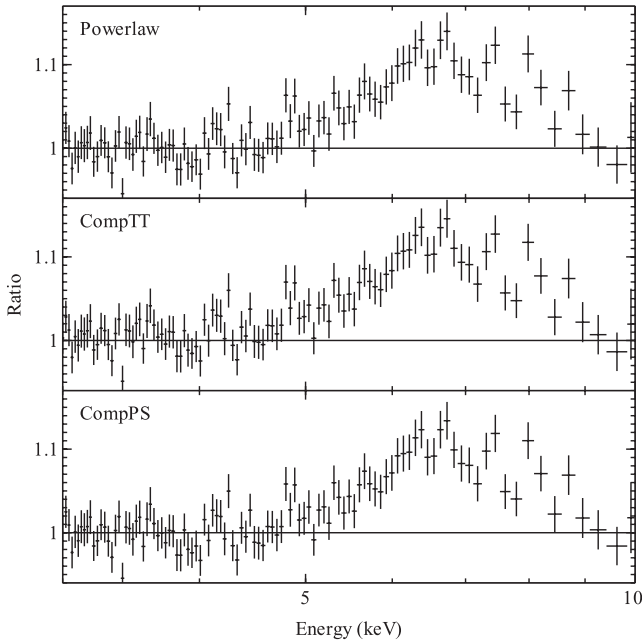
Figure 2. Data/model ratio plots for the *XMM–Newton* observation of XTE J1650−500, focusing on the iron emission, after making use of various models for the high-energy Comptonized continuum. The models investigated are a simple power law (top panel), and the COMPTT and COMPPS Comptonization codes (middle and bottom panels, respectively). The choice of model does not affect the line profile obtained.

more physical Comptonization codes COMPTT (Titarchuk 1994) and COMPPS (Poutanen & Svensson 1996). In both cases the temperature of the seed photon spectrum was set to that of the DISKBB component, and we assumed a standard slab geometry. These models were applied in the same manner detailed previously (i.e. initially excluding the 4.0–8.0 keV data), and the line profiles obtained examined. As shown in Fig. 2, the use of these more sophisticated Comptonization models does not lead to any modification of the line profile. With the addition of a LAOR2 line we obtain fits of equivalent quality to the case using the simpler power-law continuum in both cases (χ^2_ν = 1933/1660 and 1941/1660, respectively). The parameters obtained for the line profile with each of the models are given in Table 2, and show excellent agreement within their statistical uncertainties. Therefore, we conclude that a simple power-law component provides an adequate representation of the Comptonized continuum in the bandpass considered. We will proceed with the use of this approximation throughout the rest of this work. In addition, it is clear that any systematic uncertainties introduced through our choice of

Table 2. Key iron line parameters obtained when modelling Comptonized continuum with the COMPTT and COMPPS codes. The line profiles have again been modelled with a LAOR2 component, in the same manner as with the simple power-law continuum. The values obtained show excellent agreement with those presented in Table 1.

Model	E (keV)	R_{in} (R_G)	q_{inner}	i (°)
COMPTT	$6.97^p_{-0.32}$	1.5 ± 0.1	>6.6	69^{+2}_{-4}
COMPPS	$6.97^p_{-0.44}$	1.5 ± 0.1	>8.7	69^{+3}_{-7}

continuum model are negligible in comparison to the statistical parameter uncertainties obtained.

3.1.4 Disc reflection

We now embark upon a more physical consideration of the relativistic disc reflection scenario for XTE J1650−500, and replace the DISKBB and LAOR components with the REFBHB model (Ross & Fabian 2007) convolved with the KDBLUR kernel, which applies the same relativistic effects included in the LAOR line model to any general input spectrum, but assumes a simpler single power-law emissivity profile of form $\epsilon(r) \propto r^{-q}$. REFBHB is a self-consistent reflection model which intrinsically calculates the iron K-shell absorption and emission in the reflecting medium, correctly including effects such as Compton broadening, which, as emphasized previously, is an important process in BHBs due to the high temperature of the disc (Ross & Fabian 2007). It is calculated specifically for use with spectra from BHBs as it includes the thermal emission from the accretion disc. Its key parameters are the hydrogen number density and temperature of the accretion disc (n_H and kT), the photon index of the illuminating power-law continuum, the relative strength of the illumination with respect to the thermal emission at the surface of the disc (F_{il}/F_{th}) and the redshift of the reflecting medium. We assume the redshift is zero, while the photon index of the illuminating emission was required to be the same as that of the power-law continuum component. This model provides a fairly good representation of the data, with $\chi^2_\nu = 1832/1663$, and the iron line profile is well modelled. The key parameters obtained are given in Table 3 as Model 1, and the relative contributions of the components are shown in Fig. 3. As suggested by the results obtained with the LAOR2 line profile in Section 3.1.2, we again find that the inner radius of the disc is small, with $R_{in} \sim 2 R_G$, although the radius obtained here is slightly larger than with the simple LAOR2 profile, owing to the self-consistent inclusion of Compton broadening in REFBHB. In addition, the value obtained for F_{il}/F_{th} suggests that the Comptonized emission contributes significantly more to the total flux than the thermal emission from the disc, which is not uncommon for a source during the transition from the low/hard to the high/soft state (Remillard & McClintock 2006).

In order to assess whether our choice of reflection model has any major influence over the key parameter values obtained, we replaced REFBHB with REFLIONX (Ross & Fabian 2005), another self-consistent reflection code. In particular, we are interested in the inner radius of the disc, which in turn provides information on the spin of the black hole and is the key in determining the width of the line. The key parameters of REFLIONX are the iron abundance and ionization parameter (defined as $\xi = L/nR^2$, where L is the ionizing luminosity of the source, n is the density of the absorber and R is its distance from the source) of the reflecting medium, and the photon index of the ionizing continuum. We again required the photon index parameters of both the reflection model and the power-law continuum to be the same, and the iron abundance was set to the solar value. As expected, the reflecting medium is found to be highly ionized, with log $\xi = 2.8$. However, although REFLIONX includes treatment of all the same processes as REFBHB, it is calculated for use with X-ray spectra from active galaxies, and does not include the direct thermal emission from the disc in the correct fashion for BHBs. In order to account for this emission we again included a DISKBB component. This alternative reflection model is also able to reproduce the data fairly well, with $\chi^2_\nu = 1848/1662$. The inner radius obtained for the disc here is $R_{in} = 1.31^{+0.13}_{-0.07}$, even smaller than in the REFBHB case.

Table 3. Key parameters obtained for the various models constructed using a reflection interpretation for the *XMM–Newton* spectrum of XTE J1650−500 (see text); parameters marked with an asterisk (*) have not been allowed to vary. Note that when included, the Ne II and Ne III lines have been required to contribute equal amounts to the negative residuals at ∼0.85 keV. Column densities are given in 10^{21} atom cm^{-2}, abundances are quoted relative to the solar abundances, EWs are given in eV, radii in gravitational radii, inclinations in degrees, temperatures in keV and hydrogen number densities are given in 10^{20} atom cm^{-3}. For the model including the XSTAR grid, the ionization parameter is given in erg cm s^{-1}, and the outflow velocity in km s^{-1}. Note that these results are obtained with unmodified *XMM–Newton* data; for results obtained after the application of the EPFAST tool, see Section 3.1.7.

Component	Parameter	Value				
		Model 1	Model 2	Model 3	Model 4	Model 5
TBABS	N_H	$7.17^{+0.08}_{-0.09}$	$7.2^{+0.2}_{-0.1}$	$7.4^{+0.1}_{-0.2}$	$7.2^{+0.2}_{-0.1}$	$7.2^{+0.2}_{-0.1}$
	A_O		$1.06^{+0.05}_{-0.02}$	$1.26^{+0.06}_{-0.04}$	1.16 ± 0.07	$1.07^{+0.04}_{-0.06}$
	A_{Ne}	$1.36^{+0.06}_{-0.03}$	1.5 ± 0.1	$0.9^{+0.02}_{-0.3}$	1.4 ± 0.2	1.3 ± 0.2
	A_{Fe}	$0.95^{+0.04}_{-0.07}$	$0.8^{+0.2}_{-0.1}$	$0.9^{+0.2}_{-0.3}$	0.7 ± 0.2	$0.6^{+0.1}_{-0.2}$
XSTAR	N_H	–	–	–	–	1.6 ± 0.4
	ξ	–	–	–	–	100^{+20}_{-10}
	v	–	–	–	–	6000 ± 4000
Ne II (abs)	EW	–	-3.2 ± 0.5	–	-2 ± 1	–
Ne III (abs)	EW	–	-3.2 ± 0.6	–	-2 ± 1	–
POWERLAW	Γ	$2.057^{+0.003}_{-0.020}$	$2.03^{+0.02}_{-0.03}$	$2.06^{+0.01}_{-0.02}$	2.02 ± 0.03	$2.06^{+0.01}_{-0.03}$
KDBLUR	R_{in}	$2.2^{+0.2}_{-0.3}$	$1.9^{+0.6}_{-0.4}$	$1.56^{+0.06}_{-0.02}$	$1.9^{+0.6}_{-0.5}$	$1.7^{+0.3}_{-0.2}$
	R_{out}	400*	400*	400*	400*	400*
	i	55 ± 2	60^{+13}_{-10}	66^{+3}_{-1}	59^{+9}_{-7}	65^{+1}_{-6}
	q	$5.4^{+1.1}_{-0.2}$	>4.1	$7.3^{+1.1}_{-0.8}$	>4.3	7^{+2}_{-1}
REFBHB	kT	0.200 ± 0.001	0.20 ± 0.01	$0.197^{+0.001}_{-0.003}$	$0.20^{+0.02}_{-0.01}$	$0.20^{+0.01}_{-0.02}$
	n_H	$1.22^{+0.03}_{-0.04}$	$0.59^{+0.05}_{-0.06}$	$1.09^{+0.16}_{-0.08}$	$0.60^{+0.10}_{-0.03}$	$1.18^{+0.04}_{-0.30}$
	F_{il}/F_{th}	$5.0^{+0.2}_{-0.1}$	$3.2^{+0.4}_{-0.2}$	4.4 ± 0.6	$3.0^{+0.7}_{-0.3}$	$5.0^{+0.3}_{-2.1}$
O VIII (em)	EW	–	–	60^{+10}_{-30}	15^{+9}_{-13}	–
χ^2_ν		1832/1663	1721/1662	1718/1662	1713/1661	1700/1660
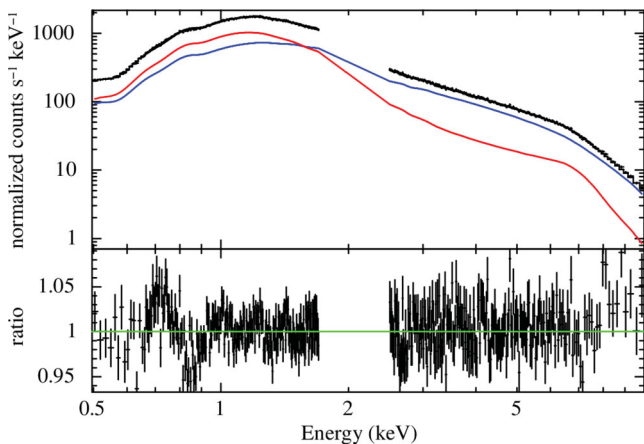
Figure 3. The basic disc reflection model (Model 1) for XTE J1650−500 presented in Section 3.1.4, and the relative contributions of the components included. The solid black line shows the total model, while the blue shows the power-law continuum and the red shows the blurred reflection component (which includes the thermal contribution from the disc). The spectra have been rebinned for clarity.

This decrease can be understood in terms of the differing situations for which the two reflection models are calculated. We stress again that REFLIONX is calculated for use with active galaxies, and therefore assumes a much cooler temperature and lower density for the accretion disc. This in turn reduces the contribution from Compton broadening, hence additional gravitational broadening is required to reproduce the line profile, and a smaller inner radius is obtained. For this reason, the inner radius obtained with REFBHB is more appropriate as it includes the correct amount of Compton broadening for XRBs.

It is worth briefly noting that the neutral column density for the ISM obtained is consistently larger than that presented in some of the previous work on this source (e.g. Miller et al. 2004; Miller et al. 2009a), possibly owing to the inclusion of data in the range 0.5–0.7 keV in our analysis. If we restrict ourselves to a consideration of the same 0.7–10.0 keV energy range analysed in Miller et al. (2009a), we obtain equivalently acceptable fits with a column density consistent with theirs. However, in doing so the abundances of oxygen, neon and iron obtained are all approximately two times solar. The difference in column obtained is therefore most likely to be due to the updated absorption models, solar abundances and cross-sections used in this work. In addition, none of the models presented required the energy of the neutral oxygen recombination edge to be shifted away from the expected value, as originally found in Miller et al. (2002).

3.1.5 Soft residuals

In both cases, the residuals at ∼0.6–0.8 keV are still present. In order to test whether these features are real, or arise due to problems with the burst mode calibration at low energies, we also briefly analyse the 2002 *XMM–Newton* burst mode observations of the Crab nebula,

obtained approximately six months after the XTE J1650−500 data presented. Data reduction was performed separately for each of the three orbits following the prescription outlined in Section 2.1, and the resulting spectra were combined again in a response-weighted manner using ADDSPEC. The final spectrum obtained was modelled with an absorbed power law, again using TBABS to model the Galactic absorption. We adopt the abundances for the ISM in the direction of the crab reported by Kaastra et al. (2009) (here adopting the solar abundances of Lodders 2003, as used in that work). The best-fitting column density and photon index are $N_H = 4.03 \pm 0.02 \times 10^{21}$ atom cm^{-2} and $\Gamma = 2.070 \pm 0.004$, although the fit quality is relatively poor, with $\chi^2_\nu = 2362/1743$. Kirsch et al. (2006) also obtained a fairly poor quality fit with a similar photon index to that obtained here. The data/model ratio plot obtained with this model is shown in Fig. 1 (Panel D). It is clear that similar residuals to those seen in the XTE J1650−500 data at ∼0.6–0.8 keV are present, although they do not appear to be as prominent. This might indeed indicate the features arise at least in part due to calibration uncertainties. Alternatively, it might indicate that they originate due to uncertainties in the absorption model used; were this to be the case the residual features observed in XTE J1650−500 might be expected to be stronger than those in the Crab given the higher column density obtained for XTE J1650−500. Therefore, we consider it likely that, at least to some extent, the soft residuals in XTE J1650−500 are due to systematic uncertainties in either the *XMM–Newton* burst mode calibration or the absorption model. It is worth noting that residual features at soft energies have been seen in a number of timing/burst mode observations of XRBs which may also indicate calibration uncertainties.[6] If we exclude the 0.7–1.0 keV energy range from our consideration, the simple reflection model (Model 1) gives a good fit, with $\chi^2_\nu = 1672/1601$.

In the interest of completeness, we also explore a number of physical explanations for the origin of these soft features, beginning here with interpretations that do not require additional absorption over that due to the ISM. However, we stress again our belief that systematic uncertainties are contributing towards the residuals, so the additional interpretations presented in this section should be treated with caution. We attempt to model the residuals as a combination of blended Ne II and Ne III absorption lines, which are not included in TBABS but frequently arise due to the ISM (Juett et al. 2006), and additional reflected O VIII emission over that expected from an accretion disc with solar abundances, similar to that seen in the ultra-compact neutron star (NS) XRB 4U 0614+091 (Madej et al. 2010). In the case of 4U 0614+091 the strong oxygen emission was explained as arising due to accretion from an oxygen-rich white dwarf. Such a scenario is not plausible for XTE J1650−500 so another source of oxygen-rich material is required here. REFBHB is calculated assuming solar abundances (as given in Morrison & McCammon 1983) so the extra O VIII emission is modelled with the addition of a narrow Gaussian at 0.654 keV to REFBHB before the relativistic effects were applied, while the neon absorption is modelled simply with two narrow Gaussian absorption lines, required to contribute equally for simplicity (the work of Juett et al. 2006 suggests this is not unreasonable.). This combination provides a good representation of the data, with an improvement of 119 for 2 extra degree of freedom, and the parameters obtained are given in Table 3 as Model 4.

On investigation, we find that either the combined neon absorption lines or the additional oxygen emission can resolve the residuals

individually, providing improvements of $\Delta\chi^2 = 111$ and 114 (for one additional degree of freedom), respectively. For comparison, the parameters obtained with these interpretations are also given in Table 3 as Model 2 and Model 3, respectively. However, in the former case the neon equivalent widths are EW $= -55 \pm 10$ mÅ (for each line), much greater than those obtained using the 2001 *Chandra* MEG spectra of XTE J1650−500 (∼−2–10 mÅ; Miller et al. 2004). In the latter, the disc inclination is strongly constrained to be high ($65 < i < 69°$), inconsistent with that obtained with a similar interpretation in Miller et al. (2009a), although we note that a different reflection code is used in this work, and the inclination obtained here is consistent with the lower limit of $50 \pm 3°$ obtained from the optical light curve by Orosz et al. (2004). We consider a combination of these features more plausible, and with this interpretation neither the inclination nor the neon EWs are as tightly constrained, due to the degeneracy between the inclination and the emissivity index when modelling the line profile, and also the degeneracy between the individual interpretations. The neon EWs may be made consistent with those presented in Miller et al. (2004) by shifting more emphasis on to the oxygen emission. However, we note that doing so tightens the requirement for a high inclination. It seems that in assigning a combination of these physical origins for the soft residuals this model can be consistent with either the inclination obtained in Miller et al. (2009a) or the neon absorption presented in Miller et al. (2004), but it cannot be consistent with both.

It is also possible that the soft residuals may indicate absorption by ionized material associated with XTE J1650−500 rather than the ISM, most likely due to an outflowing disc wind. To test this we generated a grid of ionized absorption models using XSTARV2.2.1, adopting solar abundances for all the elements and a turbulent velocity of 100 kms^{-1}. The free parameters of this model are the column density, the redshift, which may in turn be used to infer the outflow velocity, and the ionization parameter of the absorbing medium. Including this additional component in the basic disc reflection interpretation constructed previously, the model also provides a good representation of the data, with an improvement of $\Delta\chi^2 = 126$ for three additional degrees of freedom. The key parameters for this interpretation are also given in Table 3, as Model 5.

In this scenario, the residuals represent a complex blend of various narrow absorption features. The best-fitting value obtained for the redshift is *positive*, which suggests that if the material is associated with XTE J1650−500 it is *infalling*, rather than outflowing, with a velocity of 6000 ± 4000 kms^{-1} (although this is not particularly well constrained due to the blend of multiple features contributing). Given that the work of Orosz et al. (2004) strongly suggests XTE J1650−500 is a low-mass X-ray binary (LMXB), and hence mass transfer should occur through Roche lobe overflow rather than via stellar winds, the presence of such infalling material might be considered unusual, especially given the high velocity, so it is not clear if this is the correct interpretation, although it remains an intriguing possibility. Such material could be the remnant of a failed outflow, which is now falling back on to the black hole. However, even if the soft residuals are due to absorption by partially ionized matter, Fig. 4 shows that this material does not contribute any significant absorption features in the ∼3–10 keV energy range.

In summary, a number of astrophysical origins for the soft residuals provide statistically acceptable fits to the data. However, given the physical issues each of these raise (requiring unreasonably high neon absorption in the ISM and/or an unexplained over abundance of oxygen, or the presence of rapidly infalling material) and the comparison with the burst mode data from the Crab nebula, we strongly

---

[6] see http://xmm2.esac.esa.int/docs/documents/CAL-TN-0083.pdf
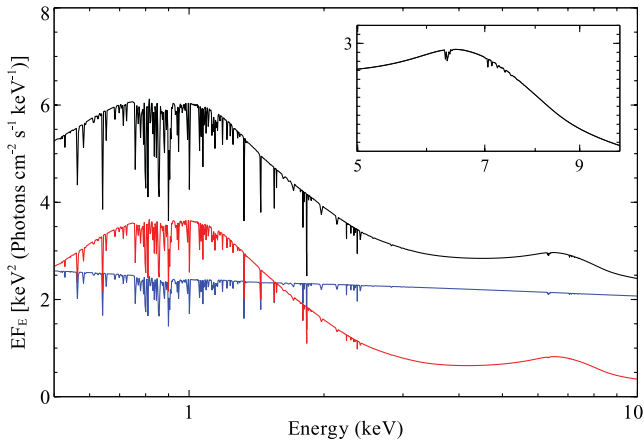
Figure 4. The model obtained treating the soft residuals as evidence for an ionized disc wind (see Section 3.1.6 and Model 5 in Table 3) through use of an XSTAR absorption grid. The total model, corrected for Galactic absorption, is shown in black, the red shows the contribution of the reflection component (including the thermal emission from the disc) and the blue shows the power-law continuum. Inset: the same model zoomed in on the 5–10 keV energy range. The ionized absorber does not contribute any strong absorption features at these energies.

suggest these features are systematic rather than astrophysical. The roughly consistent inner radius obtained with each interpretation demonstrates that they are not critical to our determination of this key parameter.

3.1.6 Ionized absorption in the iron K band

We now focus on the 5–10 keV range in order to determine whether absorption from highly ionized species could modify the obtained line profile. The only possible absorption feature in the data is at $\sim$7.1 keV. Assuming an identification with hydrogenic iron, this material would be outflowing at 6000 ± 2000 km s^{-1}, much higher than the typical velocities seen for XRB disc winds, which are less than $\sim$1000 km s^{-1} (see e.g. Lee et al. 2002; Ueda et al. 2004; Miller et al. 2006; Neilsen & Lee 2009), but not as high as the relativistic wind described in Done & Gierliński (2006) (see below). However, the detection is fairly tentative (including an unresolved Gaussian absorption line gives an improvement of $\Delta\chi^2 \sim 8$ for two extra degrees of freedom) and if real this is a weak feature (EW ~ -10 eV); its inclusion in any of the presented models does not alter the inner radius obtained. If this absorption line is real, and ionized absorption is the correct interpretation for the soft residuals, the significant difference in their velocities suggests these features cannot be associated with the same absorber.

Based on the *BeppoSAX* observation of XTE J1650−500 taken about a day before the *XMM–Newton* observation analysed here, Done & Gierliński (2006) argue that a strong, highly blueshifted absorption line at $\sim$7.6 keV may be present due to ionized iron in a relativistically outflowing disc wind, and that failing to account for this line can lead to an artificially low inner disc radius. The line can instead be consistent with a truncated disc of inner radius $\sim$10–20 R_G, although reflection of the Comptonized continuum by this disc, producing a fairly broad iron line, is still required. We extracted the *BeppoSAX* MECS spectrum in question (covering 2.5–10.0 keV), and phenomenologically modelled the 2.5–4.0 and 8.0–10.0 keV data with the basic BHB components as described in Section 3.1.1; the continuum model obtained for this observation
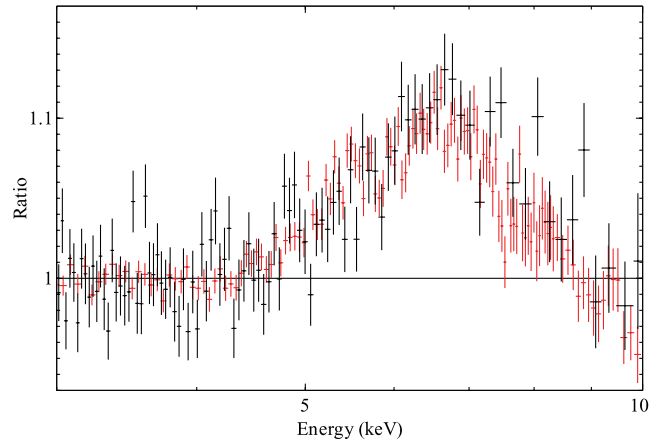
Figure 5. Iron line profiles for the *XMM–Newton* (black) and *BeppoSAX* (red) observations of XTE J1650−500, obtained on 2001 September 13 and 11, respectively. The two observations may be fitted with similar continuum models, resulting in practically identical line profiles.
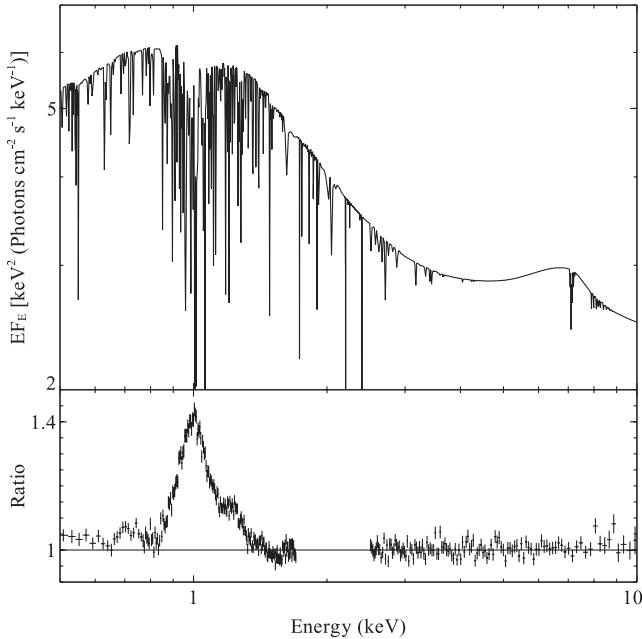
is very similar to that for the *XMM–Newton* data. A broad excess emission feature is again clearly apparent when the 4.0–8.0 keV data are included. In Fig. 5 we show both the *BeppoSAX* and *XMM–Newton* line profiles; the two are found to be practically identical.

We then verified that the MECS data, covering 2.5–10.0 keV, can indeed be consistent with a truncated disc when ionized absorption from a relativistic outflow is included, making use again of REFBHB and the XSTAR grid described above. Throughout this analysis a lower limit of 45° was imposed on the inclination, similar to the lower limit found by Orosz et al. (2004), and the same interstellar absorption as obtained with the full *XMM–Newton* data was applied. We obtained an inner disc radius of $16^{+4}_{-3}\,R_G$ for the MECS data, with absorber properties $N_H = 2.2^{+0.6}_{-0.4} \times 10^{22}$ atom cm^{-2}, $\xi = 240 \pm 60$ erg cm s^{-1} and $v_{out} = 0.138 \pm 0.007\,c$. These values are similar to those presented in Done & Gierliński (2006).

On investigation, even though there is no strong visual hint of any strong absorption in the high-energy data, we also found that the 2.5–10.0 keV *XMM–Newton* spectrum can be consistent with a similar interpretation ($R_{in} = 17^{+92}_{-9}\,R_G$), with $N_H = 10^{+8}_{-5} \times 10^{21}$ atom cm^{-2}, $\xi = 140^{+70}_{-120}$ erg cm s^{-1} and $v_{out} = 8.8^{+0.6}_{-1.0} \times 10^{-2}\,c$. However, as shown in Fig. 6 (top panel), this absorber predicts a variety of additional absorption features below 2.5 keV. Including again the 0.5–1.7 keV *XMM–Newton* data, it is clear these absorption features are not present in the data, with the model providing a very poor fit over this energy range ($\chi^2_\nu = 15477/1665$) as demonstrated by Fig. 6 (bottom panel). Finally we attempted to model the full *XMM–Newton* spectrum with this interpretation, resulting in the inner radius settling again at $\sim$2 R_G and the contribution of the absorber being minimized. Although the interpretation invoking a combination of a truncated disc and a relativistic outflow remains viable if only the 2.5–10.0 keV data are considered, the additional data below 2.5 keV provided by *XMM–Newton* exclude the presence of absorption strong enough to affect the observed width of the iron line. Therefore, we consider the inner radius of $\sim$2 R_G consistently obtained to be robust to the effects of absorption.

3.1.7 Instrumental effects

As stated previously, the residual features seen in the $\sim$1.7–2.5 keV range are most likely due to calibration uncertainties associated with the silicon K and gold M instrumental edges. These features

Figure 6. Top panel: the model obtained for XTE J1650−500 considering only the *XMM–Newton* data above 2.5 keV and including a strong relativistic outflow, similar to that proposed in Done & Gierliński (2006), in order to allow the line profile to be consistent with a truncated disc. This outflow would also imprint strong absorption features below 2.5 keV. Bottom panel: data/model ratio plot of the broad-band *XMM–Newton* spectrum to the model shown in the top panel, with the 0.5–1.7 keV data included. The low-energy absorption predicted with the inclusion of a strong, relativistic outflow is clearly not present in the data.

are most prominent for sources with high count rates, such as XTE J1650−500, and it has been suggested that this may be (at least partly) due to residual CTI.[7] This is a process that occurs during the readout of CCD detectors. As charge is transferred from one pixel to another, some of the electrons may be lost into 'charge traps' randomly distributed throughout the silicon lattice. This results in the measured energy of the incident photon being underpredicted. More recently, evidence has been found that suggests the residuals may instead be caused by X-ray loading[8] (XRL). This effect is caused by X-ray photons contaminating the offset map produced prior to each observation to determine the energy zero-point for each pixel, and hence occurs preferentially for bright/hard sources. Whatever the physical cause, the current corrections applied in the standard *EPIC*-pn data reduction procedure do not adequately describe the instrumental features for high count rates.

The EPFAST tool marks a serious effort to improve the performance of *EPIC*-pn fast-readout modes (Timing and Burst) by accounting for these remaining instrumental effects. In our reduction and analysis, we have found that EPFAST produces spectra that are better described by standard spectral responses at low energies, specifically in the 1.5–2.5 keV range where it corrects for the apparent shift of the instrumental edges very well. However, EPFAST is likely unsuited to higher energies at present, because it applies an energy-independent correction ($\Delta E/E$ = constant). Studies show that CTI depends on energy as $(\Delta E/E)_{\rm CTI} \propto E^{-\alpha}$, with $\alpha \simeq 0.5$, meaning that the relative impact of CTI is two times greater at 2 keV than
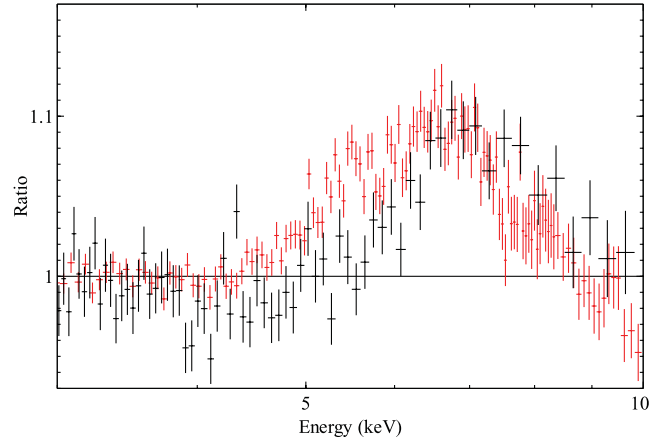
at 6–7 keV (see e.g. Gendreau, Bautz & Ricker 1993; Townsley et al. 2002; Grant et al. 2004; Prigozhin et al. 2004; Nakajima et al. 2008). Indeed, the CTI correction included in the standard reduction procedures is an energy-dependent correction, but any remaining CTI will also be energy dependent. If instead the residuals are due to XRL, the correction applied by EPFAST is an even worse approximation. To zeroth order, XRL causes a constant offset in the energy scale, i.e. ΔE = constant, therefore in this case, again writing $(\Delta E/E)_{\rm XRL} \propto E^{-\alpha}$, we have $\alpha \simeq 1$, hence the relative impact of XRL at 6 keV, in comparison to at 2 keV, is even less than for CTI. As the level of correction is primarily calibrated at ∼2 keV, especially for burst mode, EPFAST must overcorrect spectra at high energies.

This is supported by the striking difference between the *BeppoSAX* and EPFAST-modified *XMM–Newton* spectra of XTE J1650−500 in the iron *K* band (see Fig. 7). In contrast, as demonstrated by Fig. 5, the unmodified *XMM–Newton* spectrum is remarkably similar to the *BeppoSAX* data. As the *XMM–Newton* and *BeppoSAX* observations in question are only separated by a day, given the long-term evolution of XTE J1650−500 during this outburst presented by Done & Gierliński (2006), we expect any astrophysical changes displayed by XTE J1650−500 between these two observations to be minimal. The disagreement between the line profiles in the EPFAST-modified *EPIC*-pn and the *BeppoSAX* spectrum, as well as the agreement between the profiles in the latter and the unmodified *EPIC*-pn spectrum, suggests that the unmodified data may represent a better approximation of the true energy scale in the ∼6 keV energy range for count rates as high as measured in XTE J1650−500. In an attempt to quantify the comparisons presented in Figs 5 and 7 in a simple manner, we return to the Gaussian line profile considered initially in Section 3.1.2, and applied this model to both the EPFAST-modified and *BeppoSAX* data. The results obtained for these data, as well as those from the unmodified *XMM–Newton* data obtained previously, are presented in Table 4. As before, the line energies were constrained to be in the range 6.4–6.97 keV.

The line width obtained with the EPFAST-modified data is marginally smaller than that obtained with the unmodified data. Although this must be considered a systematic change, as it arises due to a redistribution of photon energies, the difference is small in comparison with the statistical uncertainty on each; the widths of

Figure 7. Iron line profiles for the *XMM–Newton* (black) and *BeppoSAX* (red) observations of XTE J1650−500, as in Fig. 5, but here the *XMM–Newton* data have been modified with the EPFAST tool. This modification results in clearly discrepant line profiles.

---

[7] See http://xmm2.esac.esa.int/docs/documents/CAL-TN-0083.pdf
[8] http://xmm2.esac.esa.int/docs/documents/CAL-TN-0050-1-0.ps

Table 4. Comparison of the results obtained for the unmodified and EPFAST-modified *XMM–Newton* calibrations and the contemporaneous *BeppoSAX* observation, when modelling the iron emission with a simple Gaussian line profile. The line widths are consistent in all cases, but only the unmodified *XMM–Newton* calibration provides a statistical agreement with the *BeppoSAX* data for the line energy (see also Fig. 8).

| Data set	E_{Gauss} (keV)	σ (keV)
BeppoSAX (September 11)	<6.41	1.09 ± 0.1
XMM–Newton (unmodified)	<6.50	$1.17^{+0.24}_{-0.21}$
XMM–Newton (EPFAST-modified)	>6.81	1.07 ± 0.25

the two profiles are fully consistent within their 90 per cent confidence limits, and both values are extremely broad. Therefore, we conclude that in this case instrumental effects do not appear to be causing a statistically significant broadening of the line profile. However, when considering the line energies obtained, only the unmodified *XMM–Newton* data are in agreement with *BeppoSAX*. The disagreement between the EPFAST-modified *XMM–Newton* and the *BeppoSAX* data is further emphasized in Fig. 8 (left-hand panel), which shows the line energy confidence contours for the two data sets. The main effect of EPFAST in this case is to shift the line profile to higher energies, without significantly modifying its width. To further demonstrate this, in Fig. 8 (right-hand panel) we again overlay the EPFAST-modified and *BeppoSAX* line profiles, but now with the former shifted down in energy by ~ 0.55 keV in order to realign the line centroids; the profiles are returned to excellent agreement. Indeed, modelling the line with a LAOR2 profile at 7.5 keV (again shifted by ~ 0.55 keV in comparison to the unmodified case) gives practically identical results to those presented in Table 1: $R_{\mathrm{in}} = 1.37^{+0.06}_{-0.02} R_{\mathrm{G}}$, $q_{\mathrm{inner}} > 8.1$ and $i = 70 \pm 1°$. Although a shift of 0.55 keV represents an energy difference of ~ 8 per cent and EPFAST only formally applies a gain shift of ~ 3 per cent in this case, in Appendix A we demonstrate that the use of EPFAST naturally leads to a much larger energy shift when

modelling a broad feature at 6.4 keV, fully consistent with that obtained, as the application of this tool modifies the high-energy continuum, which can be difficult to determine underneath such a broad line.

Based on this comparison and the theoretical considerations of the relevant instrumental effects discussed earlier, we conclude that the unmodified data do provide the best approximation of the true energy scale, while the modified data probably yield the best description of the line width. Furthermore, the good agreement of the *BeppoSAX* and unmodified *XMM–Newton* spectra suggests that even if some process other than CTI or XRL is the primary cause of the instrumental residuals at ~ 2 keV, the overall effect of this process at high energies (~ 6 keV) is small. We note briefly that if either CTI or XRL is the dominant cause of the residuals at ~ 2 keV, as appears likely, these effects could also be contributing to the soft residuals observed below 1 keV, given that the relative strength of both of these processes is higher at soft energies. These features are of little consequence for the main aim of this paper, but we again urge that the possible physical origins presented for the soft residuals be treated with caution.

In the interest of completeness, and for further comparison, we also present the results obtained with the basic reflection interpretation (Model 1) applied to the EPFAST-modified data, including the 1.7–2.5 keV energy range. An excellent fit is obtained, with $\chi^2_\nu = 1843/1840$. The values obtained for various key parameters are quoted in Table 5, and we also list again the values obtained with the unmodified data for ease of comparison. We only consider the basic reflection interpretation here given the likely systematic origin of the soft residuals. In any case, with the EPFAST-modified data it is possible to resolve these residuals merely as absorption by the Galactic ISM, although some unusual abundances are required, potentially suggesting that the energy scale below ~ 2 keV may also be incorrect. Our discussion henceforth is limited to the parameters that dictate the relativistic blurring, and hence determine the line profile: the main focus of this work.

First of all, we note the consistency of the values obtained for the inner radius; the radius obtained with the EPFAST-modified data is marginally larger, but the statistical agreement with the value obtained with the unmodified data is excellent. Given the
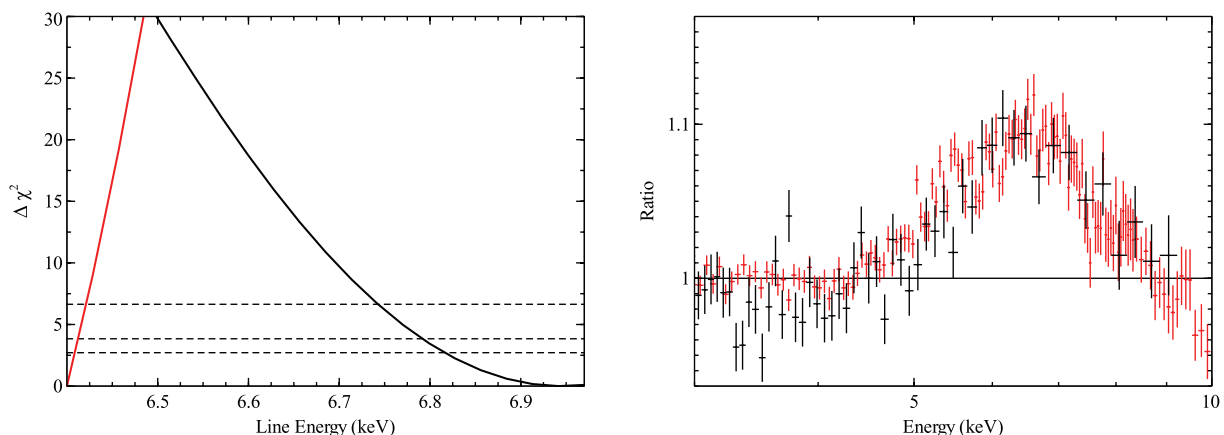
Figure 8. Left-hand panel: χ^2 confidence contours for the line energies obtained with the EPFAST-modified *XMM–Newton* (black) and *BeppoSAX* (red) data sets when modelling the iron emission with a simple Gaussian line profile. Horizontal dashed lines show the 90, 95 and 99 per cent confidence intervals for one parameter of interest. The line energies obtained with the two data sets are clearly not in agreement. Right-hand panel: comparison of the *XMM–Newton* EPFAST-modified (black) and *BeppoSAX* (red) line profiles, with the energy scale of the former shifted by ~ 0.55 keV, as suggested by the left-hand panel. Including this energy shift returns the profiles obtained to excellent agreement.

Table 5. Comparison of the parameter values obtained for the basic reflection interpretation with both the unmodified and the EPFAST-modified *XMM–Newton* data. As with Table 3, column densities are given in 10^{21} atom cm^{-2}, abundances are quoted relative to the solar abundances, radii in gravitational radii, inclinations in degrees, temperatures in keV and hydrogen number densities are given in 10^{20} atom cm^{-3}.

Parameter	Unmodified	EPFAST-modified
N_H	$7.17^{+0.08}_{-0.09}$	6.7 ± 0.1
A_O	$1.06^{+0.05}_{-0.02}$	$1.36^{+0.06}_{-0.04}$
A_{Ne}	$1.36^{+0.06}_{-0.03}$	1.7 ± 0.1
A_{Fe}	$0.95^{+0.04}_{-0.07}$	$0.52^{+0.08}_{-0.04}$
Γ	$2.057^{+0.003}_{-0.020}$	$1.99^{+0.01}_{-0.02}$
R_{in}	$2.2^{+0.2}_{-0.3}$	3 ± 1
i	55 ± 2	85^{+2}_{-11}
q	$5.4^{+1.1}_{-0.2}$	$2.0^{+0.2}_{-0.3}$
kT	0.200 ± 0.001	0.200 ± 0.002
n_H	$1.22^{+0.03}_{-0.04}$	$1.34^{+0.07}_{-0.05}$
F_{il}/F_{th}	$5.0^{+0.2}_{-0.1}$	$5.0^{+0.6}_{-0.1}$

similarly excellent agreement of the line widths when using the simple Gaussian model, this is not surprising. There are, however, two significant differences that require highlighting. The inclination is significantly higher and the index of the emissivity profile significantly lower when EPFAST is applied. This is a direct consequence of the line profile being shifted to higher energies by EPFAST. As we are using a physically self-consistent reflection model, the intrinsic energy of the iron emission is hardwired into the model, and only the blurring kernel (KDBLUR) is able to change the energy at which the emission is observed. In order to shift the line to higher energies, the blurring kernel must both enhance the blue wing (increase the inclination) and attempt to suppress some of the red wing (decrease the emissivity index) of the line profile. The best-fitting inclination obtained using the EPFAST tool is unphysically high, implying that we are observing the source practically through the plane of the disc, although the 90 per cent confidence limit does extend to slightly less extreme inclinations. Therefore, the incorrect energy scale of the EPFAST-modified data at high energies can have a significant impact on key physical parameters when using physical rather than phenomenological models. We stress again that these changes are not physical, and are purely a result of the line profile being incorrectly shifted to higher energies when the EPFAST tool is applied.

To summarize briefly, we have investigated in detail the application of the EPFAST tool, which was designed to correct the instrumental features observed in *EPIC*-pn data around ∼2 keV at high count rates. The correction applied by EPFAST does not – at the time of writing – have the correct energy dependence for either CTI or XRL, the two likely physical causes of these features, and although this does not lead to any significant changes in the width of the observed line profile in this case – which is ultimately the main focus of this work – it does result in an incorrect energy scale at high energies. As demonstrated through comparison with a contemporaneous *BeppoSAX* observation and our simulations in Appendix A, EPFAST incorrectly shifts the line profile to higher energies. This energy shift can have important implications for key parameters when using physically self-consistent reflection models in which the line

energy is not a free parameter. We will proceed henceforth with the use of the unmodified *XMM–Newton* data.

3.1.8 Alternative scenarios

Until now we have been considering the case in which the line arises due to reflection close to the black hole and is broadened by the relativistic effects present in such a region. This model therefore requires that the accretion disc, which in this scenario is the reflector, extends in (or close to) to the ISCO. However, as stated previously, there is some debate over whether this is the case at low accretion rates (specifically in the low/hard state). Having demonstrated that the line is not artificially broadened by instrumental effects, we now investigate whether the line can be primarily broadened by some other physical mechanism. The main alternative is that broadening via electron scattering (Compton broadening) dominates. This process gives a line width per scattering, σ, of

$$\frac{\sigma}{E} \simeq \left(\frac{2kT_e}{m_e c^2} \right)^{0.5}, \tag{2}$$

where E is the energy of the line and T_e is the electron temperature (Pozdnyakov, Sobol & Syunyaev 1983). In addition to broadening discrete features, Compton scattering also amplifies the energy centroid by

$$\frac{E_{obs}}{E_{int}} = 1 + 4 \left(\frac{kT_e}{m_e c^2} \right) + 16 \left(\frac{kT_e}{m_e c^2} \right)^2 + \cdots, \tag{3}$$

where E_{obs} and E_{int} are the observed and intrinsic line energies, respectively. Considering the likely geometry and processes occurring in BHBs, Compton broadening could potentially occur in three separate media: the disc itself, the corona or some outflowing disc wind. We will consider these three cases individually.

First we consider the scenario in which the breadth of the line is primarily due to Compton broadening in the corona. Modelling the line with a Gaussian profile, we obtained a line energy of ∼6.4 keV and a width of $\sigma \sim 1.1$ keV (see Sections 3.1.2 and 3.1.7). As there is no obvious narrow component to the line profile, invoking Compton broadening as the origin of its width requires that the optical depth of the corona $\tau \gtrsim 1$, i.e. the vast majority of the line photons must experience at least one scattering. Here, we consider the simplest case, in which $\tau \sim 1$ and the line is broadened by a single scattering process. Substituting the values obtained from the Gaussian profile into equation (2) we find that, in order for this to be the case, $kT_e \simeq 6$ keV. If we wish to invoke multiple scatterings, i.e. increasing the optical depth, in order to obtain the same line width, T_e would have to be lower still. However, we remind the reader that Comptonization of the line in the corona reduces its observed EW by a factor of e^τ (see Petrucci et al. 2001), so the case with $\tau \sim 1$ is the most reasonable.

A corona with $\tau \sim 1$ and $kT_e \sim 6$ keV would produce a curved continuum in the *XMM–Newton* bandpass. However, in Section 3.1.3 we demonstrated that the continuum is power-law like, with minimal curvature. To further demonstrate that such a continuum is not observed, Fig. 9 shows the confidence contours for τ and kT_e when modelling the high-energy spectrum with a combination of COMPTT and a Gaussian emission line. A combination of $\tau \sim 1$ and $kT_e \sim 6$ keV is clearly excluded. In addition, considering equation (3), Comptonization of the line in such a corona should shift the line centroid to ∼6.75 keV (assuming an initial energy of 6.4 keV). However, the line energy is constrained to be below 6.5 keV. Therefore Compton broadening in the corona does
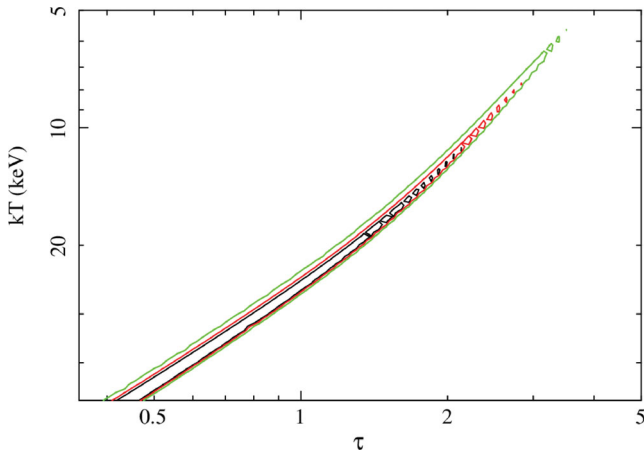
Figure 9. χ^2 confidence contours for the optical depth (τ) and electron temperature (kT_e) obtained for the Comptonizing medium with COMPTT for the *XMM–Newton* observation of XTE J1650−500. The contours shown represent the 90 (black), 95 (red) and 99 (green) per cent confidence contours for two parameters of interest.

not produce a self-consistent interpretation for both the line profile and the observed continuum. It is worth noting that Hiemstra et al. (2011) present a similar consideration for the high-energy spectrum of XTE 1652−453, and also conclude that the line profile in that source cannot be explained by Compton broadening in the corona.

Secondly, we consider electron scattering in the disc itself. As previously noted, this can be an important process in BHBs given their high disc temperatures. Indeed, we stress again that the reflection model used here, REFBHB, has been calculated specifically for use with spectra from XRBs, and self-consistently includes this process at an appropriate level for such sources. In order to demonstrate that relativistic effects are preferred over Compton processes in the disc, in Fig. 10 we show the χ^2 confidence contours for the inner radius up to $100\,R_G$ for each model presented in Table 3. In addition, we also show the case of the basic reflection model but with the ∼0.7–1.0 keV data excluded, referred to as Model 1*, to demonstrate that the presence of the soft residuals has little effect on the value obtained for the inner radius with this model. Increasing the inner radius has the effect of shifting the emphasis from a combination of Doppler and gravitational broadening to a combination of Doppler and Compton broadening. Clearly a small inner radius, and therefore the former scenario, is favoured at greater than 99 per cent confidence in each case. Furthermore, Reis et al. (2009a) demonstrate that solutions invoking highly ionized reflection at large distances from BHBs are not physically consistent with the expectation of a standard thin disc.

Finally, we also briefly consider the possibility that the line is not produced by a reflection process in the disc, but is instead produced via reprocessing of the X-rays from the central source in an outflow, then broadened by electron scattering as it escapes from the outflowing medium (see e.g. Titarchuk et al. 2009). Such a model may statistically reproduce the line profiles observed in a variety of NS and black hole XRBs. However, as shown by Cackett et al. (2010), when considered in detail there are a number of issues with this 'windline' interpretation. We refer the reader to that work for the full discussion, and merely summarize the main points here. First and foremost, in order to reproduce the line profiles observed the outflows must be optically thick. However, broad iron lines are

observed in XRBs across a broad range in inclination, hence if such lines are produced in a disc wind these outflows must cover a large solid angle. This is in contrast with both theoretical simulations of disc winds and observational evidence for absorption by such outflows; see Section 4 for a full consideration of the (lack of) connection between broad emission lines and disc winds.

In addition, the mass outflow rates obtained in Titarchuk et al. (2009) for the BHB GX 339−4 and the NS XRB Ser X-1 are both comparable with the Eddington mass accretion rate. However, in the observations analysed in that work both sources are known to be accreting comfortably below the Eddington limit, so the mass outflow rate required by the windline interpretation exceeds the mass inflow rate due to accretion.[9] Furthermore, broad iron lines are observed in NS XRBs across at least two orders of magnitude in luminosity, therefore the high-mass outflow rate would need to be independent of the accretion rate. This requirement is further supported by the lack of significant evolution in the line profile with accretion rate displayed by XTE J1650−500 (see Section 3.1.9) and XTE J1752−223 (Reis et al. 2011). Finally, broad lines and high-frequency quasi-periodic oscillations (HFQPOs) are observed simultaneously in NS XRBs (see e.g. Cackett et al. 2009). For any viable HFQPO formation mechanism, their presence dictates that the inner disc must be directly observed, rather than obscured by an optically thick outflow. In addition, Hiemstra et al. (2011) argue that it is difficult to reconcile a Compton thick outflow with a Compton thin corona. Taking all this into consideration, we conclude that the windline interpretation is not a viable solution for the presence of broad iron lines in XRBs.
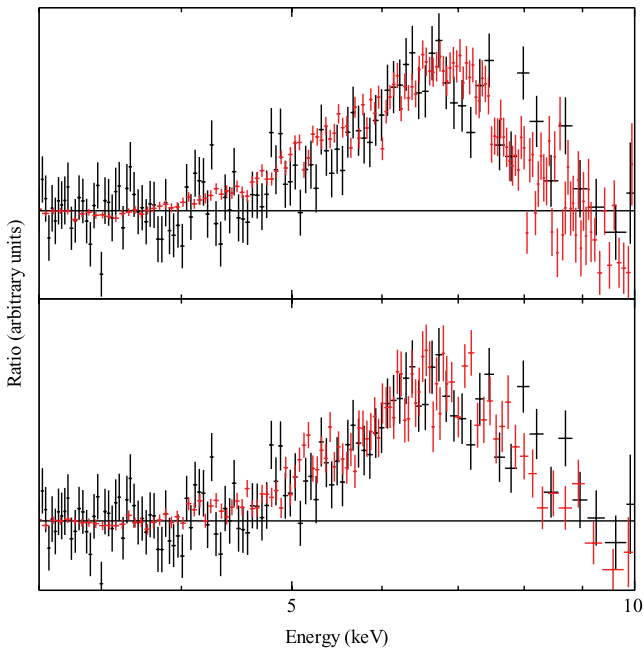
3.1.9 Line profile evolution

If the line is primarily broadened by Comptonization in either the corona or a truncated disc, which moves in as the outburst progresses through the transition from the low/hard to the high/soft state, some evolution in the width of the line profile is expected as gravitational effects become more important, and the temperature of both the disc and the corona changes (typical electron temperatures are $kT_e \sim 50$–100 keV in the low/hard state and $kT_e \sim 30$–50 keV in the high/soft state; see e.g. Sunyaev & Titarchuk 1980; Gierliński et al. 1999; Malzac & Belmont 2009). In order to determine whether any such evolution occurs we now also consider the line profiles obtained for the latter two *BeppoSAX* observations. We model the continuum in the same way detailed previously, with the same standard BHB components, requiring the photon index to be in the range 1.7–3.0. In Fig. 11 we show a comparison of the *XMM–Newton* line profile to the profiles obtained in the second and third *BeppoSAX* observations (top and bottom panels, respectively), similar to Fig. 5, although here the strength of the iron line relative to the continuum has changed, so the ratios have been scaled to match the continuum and the peak of the emission. Again, the profiles appear to have a similar breadth and shape in both cases.

Since in these cases the shape of the continuum is significantly different from observation to observation, we also quantify the comparison by modelling the iron lines from all four observations with a LAOR profile (given that the additional parameters included in the LAOR2 model could not previously be constrained we have adopted

---

[9] Although the authors of that work make a claim to the contrary, they incorrectly compare the mass outflow rate to the inflow rate for the high/soft state, despite the wind parameters being obtained for low/hard state observations, in which the accretion rate is much lower.
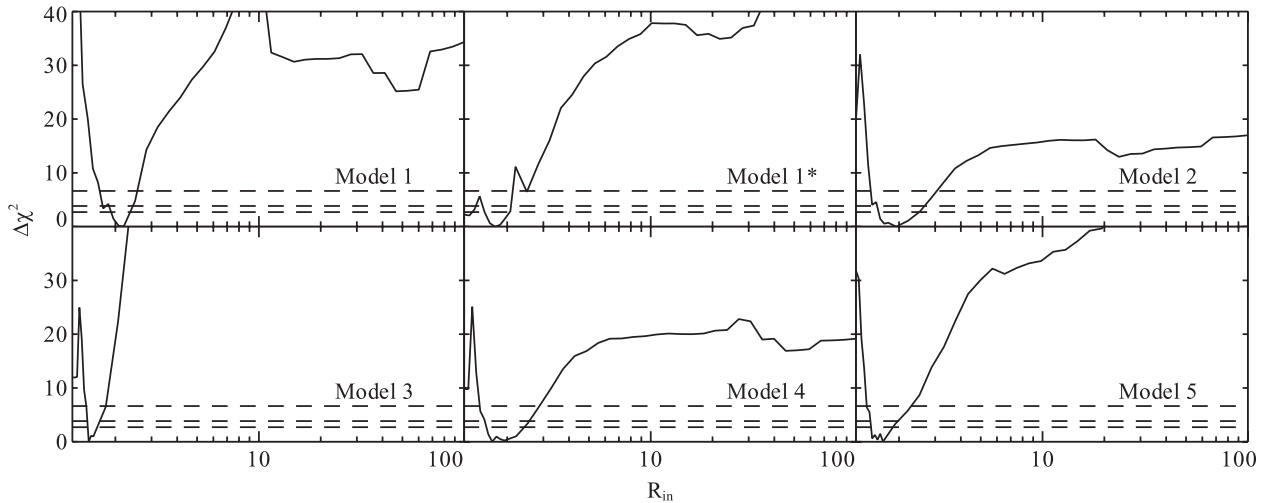
Figure 10. χ^2 confidence contours for the inner radius for each model presented in Table 3. The horizontal dashed lines represent $\Delta\chi^2$ equivalent to the 90, 95 and 99 per cent confidence intervals. Small values for the inner radius are significantly favoured in each case.

Figure 11. Comparison of the iron line profiles for the *XMM–Newton* (black) and the latter two *BeppoSAX* (red) observations of XTE J1650−500 (September 21 and October 3; top and bottom panels respectively). Again, the profiles appear to have similar breadth. A quantitative comparison is given in Table 6, confirming the similarity.

Table 6. Evolution of the inner radius for the *BeppoSAX* and *XMM–Newton* observations of XTE J1650−500 during its 2001 outburst, obtained by modelling the iron K line with a LAOR emission line profile.

Observation date	Instrument	$\dfrac{R_{in}}{R_G}$
September 11	*BeppoSAX*	$1.52^{+0.02}_{-0.03}$
September 13	*XMM–Newton*	1.63 ± 0.04
September 21	*BeppoSAX*	1.31 ± 0.01
October 3	*BeppoSAX*	$1.31^{+0.05}_{-0.04}$

a similar lack of evolution is displayed by XTE J1752−223 (Reis et al. 2011), so such behaviour is not restricted to this individual source.

3.1.10 Black hole spin

As we have demonstrated that the line profile is not modified by instrumental effects, and that relativistic disc reflection is strongly favoured over scenarios dominated by Compton broadening, we now present a quantitative measurement of the spin of XTE J1650−500, replacing KDBLUR with the KERRCONV convolution model (Brenneman & Reynolds 2006). KERRCONV applies the same relativistic effects as KDBLUR, assuming a broken power-law emissivity profile (as in equation 1), but directly includes the dimensionless black hole spin as a parameter, defined as $a^* = cJ/GM^2$, where J is the angular momentum and M the mass of the black hole, so that it must be in the range $[-1,1]$ where $a^* = 1$ is maximal prograde rotation. Its other parameters are the indices and the break radius of the emissivity profile, the inclination of the disc and its inner and outer radii. In this model the inner radius is given in terms of the ISCO, and we obtain the spin of the black hole by assuming the disc extends all the way down to this radius. We again make the simplification of a single power-law emissivity profile by requiring the two indices to be identical and assigning the break radius some arbitrary value, and the outer radius of the disc is again set as the maximum value accepted by the model. The black hole spin, the index of the power-law emissivity profile and the disc inclination were allowed to vary.

the simpler version, which assumes a single power-law emissivity profile). In this case, we model all four observations simultaneously, requiring only that the inclination does not vary between them (although the line energies are again constrained to be between 6.4 and 6.97 keV). The evolution of the key parameter in determining the width of the line, R_{in}, is shown in Table 6. Although there is some slight variation between observations, the inner radii obtained are all very similar, confirming the visual suggestion that there is minimal evolution of the line profile during the progression of the outburst. This lack of evolution strongly favours the interpretation in which the iron line arises through reflection from the inner regions of a disc with a constant and stable inner radius. We also note again that

Table 7. Black hole spin parameters obtained by replacing KDBLUR with KERRCONV for the five models given in Table 3. The spin measurement for the basic reflection model is calculated both including (Model 1) and excluding (Model 1*) the 0.7–1.0 keV data to assess the effect of the residuals on the spin measurement.

	a^*
Model 1	$0.93^{+0.02}_{-0.01}$
Model 1*	$0.96^{+0.01}_{-0.04}$
Model 2	$0.96^{+0.01}_{-0.12}$
Model 3	$0.978^{+0.002}_{-0.007}$
Model 4	$0.95^{+0.03}_{-0.08}$
Model 5	$0.97^{+0.01}_{-0.02}$

In each case, the models including KERRCONV provided statistically equivalent representations of the data as those using KDBLUR, without significant differences in any of the common parameters. The spin measurements obtained are given in Table 7, and the χ^2 confidence contours are shown for each model in Fig. 12. We again show the spin measurement and contour for the basic reflection model with the 0.7–1.0 keV data excluded (Model 1*) to investigate the effect of the soft residuals on the spin value obtained with this model. Clearly, the presence of these features does not significantly modify the spin obtained, as the values obtained including and excluding these data are consistent within their statistical uncertainties. In all cases the black hole is rapidly rotating, but maximal spin is ruled out at the 90 per cent level. To summarize, the overall constraint placed using REFBHB is $0.84 \le a^* \le 0.98$, although we note that if, as expected, the soft residuals are not astrophysical the lower limit on the spin increases as only Model 1 and Model 1* then provide valid estimates.

The spin estimates presented here are slightly higher than the value of $a^* = 0.79 \pm 0.01$ presented for the same data set in Miller et al. (2009a). On investigation, we find that this is primarily due to the different reflection codes used in these works; Miller et al. (2009a) make use of the CDID reflection code (Ballantyne, Ross & Fabian 2001), while here we use REFBHB, an adaptation of the more recent REFLIONX code which has specifically been calculated

for use with BHBs. REFLIONX (and hence REFBHB) includes a far more comprehensive range of ionized species for the elements with high cosmic abundance. These two codes use different energy ranges for the incident continuum, which may have an effect on the reflection spectrum produced. Upon replacing REFBHB with a combination of CDID and various multi-colour disc models we also obtain lower values for the spin of XTE J1650−500, consistent with those presented in Miller et al. (2009a). More recently, the reflection code XILLVER (García & Kallman 2010) has further extended the range of ionized species and atomic transitions considered, but results obtained with the use of that reflection code are typically in good agreement with those obtained with REFLIONX when considering relativistically broadened scenarios. Since there is no version of XILLVER calculated specifically for use with BHBs currently available, we do not make use of that code here.

3.2 MCG–6-30-15

Having demonstrated that the line profile observed in XTE J1650−500 has an astrophysical origin, and that the data significantly prefer the interpretation in which relativistic effects dominate, we now consider the case of the active galaxy MCG–6-30-15.

3.2.1 Continuum modelling

We began by modelling the spectrum of MCG–6-30-15 with the standard AGN power-law-like Comptonized continuum. However, the 0.5–10.0 keV X-ray spectra of active galaxies are rarely featureless. Type 1 AGN commonly display additional emission at soft energies (see e.g. Gierliński & Done 2004; Crummy et al. 2006; Miniutti et al. 2009). In order to phenomenologically account for this soft excess, we also included a blackbody emission component. Both of these were modified by neutral absorption. As MCG–6-30-15 is an extragalactic source, we initially allowed for both Galactic and intrinsic absorption with two TBABS components, one local component and the other at the redshift of MCG–6-30-15 ($z = 0.007749$; Fisher et al. 1995). The Galactic column used was 3.92×10^{20} atom cm^{-2}, based on recent 21 cm measurements (Kalberla et al. 2005),
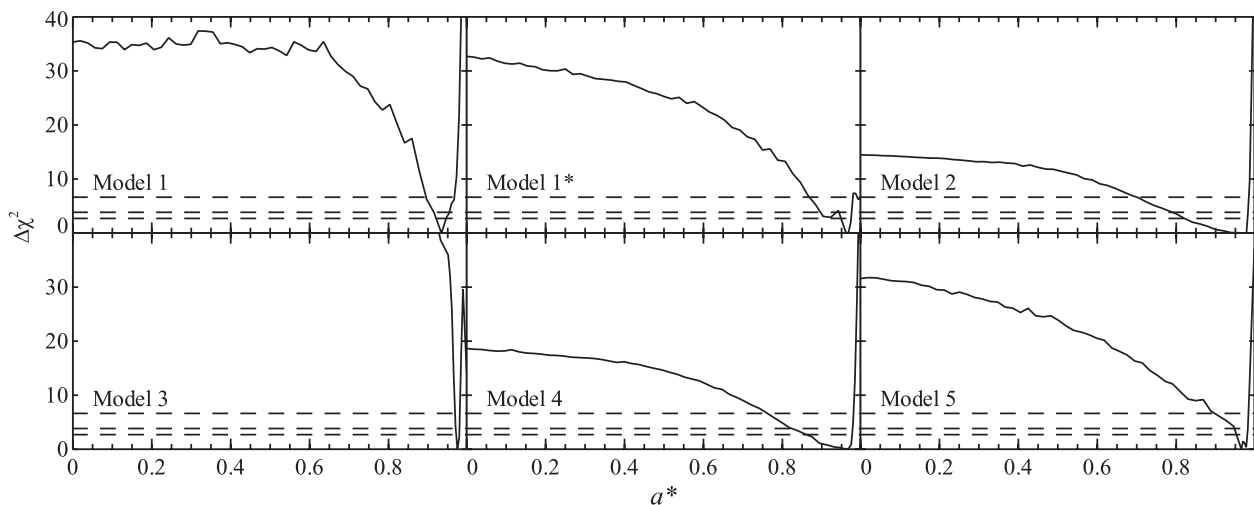
Figure 12. χ^2 confidence contours for the spin parameter measurements presented in Table 7, demonstrating the spin values presented in Table 7 are the global minima across the allowed range of values for a^*. Horizontal dashed lines represent $\Delta\chi^2$ equivalent to the 90, 95 and 99 per cent confidence intervals.

while the intrinsic column was free to vary. However, in the course of the modelling we found that the intrinsic neutral component was not required, and so was removed.

As has been widely reported in previous work (see e.g. Ballantyne, Weingartner & Murray 2003b; Young et al. 2005; Miller et al. 2008; Chiang & Fabian 2011), the spectrum of MCG–6-30-15 also displays clear signatures of ionized absorption. To account for these features, we include a model for the ionized absorber based on that of Chiang & Fabian (2011). In brief, this is a three-zone absorber which also includes a treatment of the iron-L dust absorption (Lee et al. 2001). The absorber consists of a highly ionized, rapidly outflowing absorption zone ($\log \xi \sim 3.82$, $v_{out} \sim 1900$ km s^{-1}), and two moderately ionized, mildly outflowing zones ($\log \xi \sim 2.3$ and 1.3, $v_{out} \sim 150$ km s^{-1}). These are individually included using the XSTAR photoionization code, while the iron-L dust absorption is accounted for with the inclusion of an additional TBABS component. As with XTE J1650−500, the 4.0–8.0 keV data were not considered so that the continuum was determined with minimal contribution from the iron line region. This model provides a good representation of the remaining data, with $\chi_\nu^2 = 1101/934$.

3.2.2 Line profile

As with XTE J1650−500, we now include the 4.0–8.0 keV data. Fig. 13 (top panel) shows the data/model ratio of the full MCG–6-30-15 0.5–10.0 keV spectrum to the continuum model determined in the previous section. Again, it is clear that there is a large, broad excess in the ratio spectrum in this energy range, very similar to that seen in XTE J1650−500. We again include a LAOR2 line to model this feature as a relativistically broadened iron fluorescence
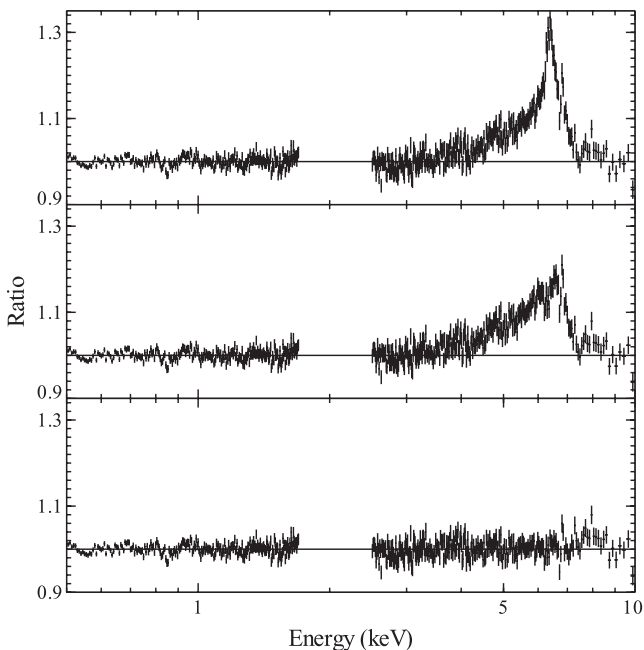
Figure 13. Data/model ratio plots for MCG–6-30-15. Top panel: ratio plot to the continuum model fit to the 0.5–4.0 and 8.0–10.0 keV data (see text); the combined profile of the broad and narrow iron emission components is clearly shown. Middle panel: ratio plot with no contribution from the LAOR2 line to demonstrate the profile of the broad line. Bottom panel: the ratio plot when both LAOR2 and Gaussian emission lines are included in the model; the iron emission is now clearly well modelled. The spectra have been rebinned for clarity.

emission line from the inner regions of the accretion disc. The rest-frame energy of the emission line was again constrained to be between 6.4 and 6.97 keV, the outer radius of the disc was taken to be 400R_G, and the rest of the line parameters were free to vary. However, in this case, the LAOR2 line did not completely account for the shape of the emission feature, due to the additional presence of a narrow core to the iron emission, which can clearly be seen in Fig. 13 (top panel). This was modelled with a Gaussian emission line at 6.4 keV (rest frame); narrow components to the iron emission in AGN can arise due to reflection from more distant, cold material, e.g. the dusty torus, or due to re-emission from photoionized clouds in the broad line region. With the inclusion of these components, the model provides a good representation of the data, with $\chi_\nu^2 = 1817/1725$. The key parameters obtained are given in Table 1 and the data/model ratio plot is shown in Fig. 13 (bottom panel). In order to demonstrate the profile of the broad iron emission, Fig. 13 (middle panel) also shows the data/model ratio with no contribution from the LAOR2 line.

This simple analysis demonstrates the similarity of the broad excesses observed in both the stellar mass BHB XTE J1650−500 and the AGN MCG–6-30-15. In both cases these excesses are consistent with a relativistically broadened iron emission line, originating from the inner regions of the accretion disc around a rapidly rotating black hole. We will now proceed to explore this similarity in more detail.

4 DISCUSSION AND COMPARISON

We have analysed the 2001 *XMM–Newton* and *BeppoSAX* observations of XTE J1650−500. In agreement with previous works on these observations, we find that this source displays a broad excess around ∼7 keV over the standard disc-plus-Comptonization model for BHBs (see e.g. Miller et al. 2002; Miniutti et al. 2004; Miller et al. 2009a). The profile of this excess is not particularly dependent on the choice of continuum model. Such excesses are frequently observed in other non-quiescent BHBs with high-quality data, and are usually interpreted as iron emission lines excited through illumination of the disc by the Comptonized continuum, then broadened and skewed by the relativistic effects present close to the compact object. We have confirmed that such disc reflection models can successfully reproduce the observed data, both phenomenologically and through the use of the more physical reflection model REFBHB (Ross & Fabian 2007). Although the basic reflection model provides a good representation of the broad-band shape of the spectrum, there appear to be residual features at ∼0.8 keV in the *XMM–Newton* data (see Fig. 1). Through a brief analysis of the 2002 *XMM–Newton* burst mode observations of the Crab nebula we find that qualitatively similar residuals are present. We therefore expect that, at least to some extent, these features are due to systematic uncertainties in either the *XMM–Newton* burst mode calibration or the ISM absorption model used, although in the interest of completeness we also explore a number of possible physical origins (see Section 3.1.5). The exact origin of these residual features is not particularly important to our broader discussion of the sources analysed in this work, as even if these residuals are evidence for absorption by ionized material, this material does not have any significant impact on the high-energy spectrum around the iron K shell transitions (see Fig. 4).

In addition, we have also briefly analysed the long 2001 *XMM–Newton* observation of MCG–6-30-15. These observations of XTE J1650−500 and MCG–6-30-15 were selected because they represent some of the highest quality X-ray data sets available for XRBs and AGNs, respectively, and previous work on these
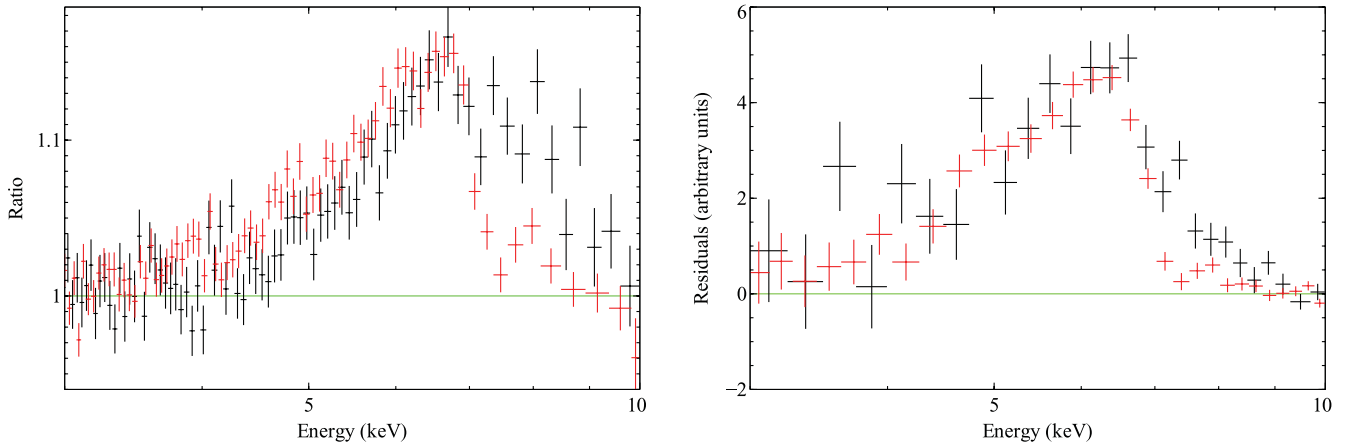
Figure 14. Data/model ratio (left-hand panel) and Data–Model residual (right-hand panel) plots for the 2001 *XMM–Newton* observations of XTE J1650−500 (black) and MCG–6-30-15 (red), highlighting the broad iron emission lines. Residuals are in units of (normalized) count s^{-1} keV^{-1}; those for MCG–6-30-15 should be multiplied by 10^{-2}. The spectra have been rebinned for clarity. Aside from differences in the blue wings which imply different disc inclinations, the line profiles are quite similar.

sources invoking relativistic disc reflection has indicated that both are likely to be rapidly rotating (see Miller et al. 2009a, and Brenneman & Reynolds 2006 for XTE J1650−500 and MCG–6-30-15, respectively). We have demonstrated that even after accounting for the ionized absorption present in MCG–6-30-15, it also appears to show a broad excess at ~6–7 keV. Although we limit ourselves to a phenomenological analysis of this source, this is sufficient for our needs, and we again show that this excess can also be modelled as a relativistically blurred iron emission line arising in the inner regions of the accretion disc due to reflection of the intrinsic Comptonized continuum.

However, these simple demonstrations are not the main focus of this work; reflection interpretations very similar to those constructed here have previously been proposed for both of these sources, using both these observations and others, and have been shown to be successful (XTE J1650−500: Miller et al. 2002; Miniutti et al. 2004; Miller et al. 2009a; MCG–6-30-15: Fabian et al. 2002; Fabian & Vaughan 2003; Ballantyne, Vaughan & Fabian 2003a; Vaughan & Fabian 2004; Reeves et al. 2006; Brenneman & Reynolds 2006; Miniutti et al. 2007). In broad agreement with these previous works, our analysis indicates the black holes powering both sources are indeed likely to be rapidly rotating, although our quantitative spin measurements for XTE J1650−500 are typically higher than that obtained by Miller et al. (2009a). As previously stated, in the case of MCG–6-30-15 partially covering absorption has also been shown to provide a good representation of the observed energy spectrum and variability when allowed sufficient complexity (Miller et al. 2008; Miller, Turner & Reeves 2009b). In this interpretation, the curvature at ~4 keV is due to the blue wing of a wide absorption trough rather than relativistically broadened emission. Inoue & Matsumoto (2003) and Miyakawa et al. (2009) propose similar interpretations, in which a relativistically broadened iron line is not required, and the variability is dominated by changes in the absorbers.

Even with the quality of data available for MCG–6-30-15 the disc reflection/light bending and partially covering/variable absorption interpretations remain statistically indistinguishable. Instead the main focus of this work is to present a comparison between the apparent profiles of the excesses observed at ~6–7 keV in these two sources, which we argue favours the reflection interpretation for this feature in AGN. We stress that this is not a proof but merely a series of logical arguments and comparisons which we find compelling,

and present here to the reader. However, this is not a statement against complex absorption in AGNs. There is clear evidence for ionized absorption in the example of MCG–6-30-15 used here. We are merely arguing that this process is not the correct origin for the feature at ~6 keV interpreted here as a broad iron emission line.

It is clear from Table 1 that the values for the key parameter in determining the red wing of the iron line, R_{in}, obtained for XTE J1650−500 and MCG–6-30-15 are similar. In Fig. 14 we focus on the line profiles of the two sources. A visual inspection shows that, aside from minor differences in the blue wings due to the different inclinations at which we are observing the inner discs of these sources, the two profiles are indeed very similar. Specifically, we draw the readers' attention to the similarity in the curvature at ~4–5 keV, which is interpreted here as the onset of the relativistically broadened iron emission line. This curvature plays a strong role in determining the inner radius of the accretion disc, so after a visual comparison it is not surprising that similar inner radii are obtained. Given the similarity of the observed profiles in these two sources, it is natural to assume that they arise from the same physical process. Since the two sources considered are separated by many orders of magnitude in terms of their black hole mass, this process must be mass independent, and is hence likely to be atomic. Indeed, we have already stressed that such excesses are commonly observed in AGN and BHBs. In addition, fairly broad excesses are also observed in NS XRBs (see e.g. Reis, Fabian & Young 2009b; Cackett et al. 2010; D'Aì et al. 2010; Lin, Remillard & Homan 2010).

4.1 Complex absorption

We have already stressed that both disc reflection and partially covering absorption provide statistically acceptable representations of the available data for MCG–6-30-15 (in the absorption case the curvature at ~4–5 keV is due to the blue wing of an absorption trough rather than excess emission.). Indeed, both of these interpretations are atomic in nature, and should therefore be mass independent. Given their relative proximity, Galactic XRBs are the ideal testing ground to determine the origin of these excesses. They are bright enough that the absorption may be very well constrained, hence we now consider the possible origins of, and observational evidence for, absorption in XRBs, with particular reference to XTE J1650−500. It is well known that the ISM contains a

combination of neutral and ionized material. However, the Galactic column is not sufficiently high for the partially ionized species to significantly alter the X-ray spectra of Galactic sources; this has been demonstrated with detailed studies of a number of sightlines (Juett, Schulz & Chakrabarty 2004; Juett et al. 2006). In addition, it is well accepted that this absorption should not vary significantly from epoch to epoch. Considering the source itself, although the masses of the black hole and its companion star have yet to be well constrained, the work of Orosz et al. (2004) strongly suggests XTE J1650−500 is an LMXB, and hence accretes via Roche lobe overflow rather than through stellar winds, so the X-ray spectrum will not suffer from obscuration due to such outflows. Many of the other XRBs (NS or black hole) that show evidence for a broad excess emission component at ∼6–7 keV are also LMXBs, and hence should also be uncomplicated by strong stellar winds from their companions.

The only other major source of material that could significantly obscure the source are outflows from the disc itself. Radiatively driven disc winds are expected to become increasingly important as black holes approach (and possibly exceed) the Eddington Limit (see e.g. King & Pounds 2003). Hydrodynamic simulations of such winds (on all scales, from AGN accretion discs to early proto-planetary discs) suggest these outflows should most severely modify the observed X-ray spectra at high inclination angles (i.e. shallow angles with respect to the surface of the disc; see e.g. Proga, Stone & Kallman 2000; Proga & Kallman 2002, 2004; Schurch, Done & Proga 2009; Owen et al. 2010; Sim et al. 2010, etc). The exact angle at which these winds become important must depend on the mass and the Eddington fraction of the black hole, which will in turn play an important role in determining the ionization structure and the mass outflow rate of the winds. For a 10^8 M$_\odot$ AGN at an Eddington fraction of $L_E = 0.5$, Schurch et al. (2009) find that the wind should start to appreciably modify the observed X-ray spectra at inclinations greater than ∼60°. We obtain a similar inclination for XTE J1650−500, and yet find no evidence for a similar level of absorption, although we note that the Eddington fraction of XTE J1650−500 in this observation is likely to be comfortably lower than that considered in Schurch et al. (2009): assuming M_{BH} ∼ 5 M$_\odot$ gives L_E ∼ 0.1.

Orbital parameters obtained for Galactic XRBs through optical studies of the companion stars indicate they are observed at a large range of inclination angles (see e.g. Orosz 2003). Although we do not find any strong evidence here, ionized absorption associated with outflowing material *is* seen relatively frequently in LMXBs, with notably strong examples being GRO J1655−40 (Miller et al. 2006; Díaz Trigo et al. 2007) and GRS 1915+105 (Kotani et al. 2000; Lee et al. 2002; Neilsen & Lee 2009; Ueda, Yamaoka & Remillard 2009). As expected, this absorption is more prominent in high inclination sources, and/or those observed at high Eddington fractions. Even at relatively high inclinations, the absorption usually manifests itself as weak, narrow line features best studied with grating spectrometers, although XRBs with the highest inclinations frequently show 'dips' in intensity, during which the absorption increases and, in some cases, can severely modify the spectrum (see e.g. Sidoli et al. 2002; Boirin et al. 2005; Díaz Trigo et al. 2006).

The general picture is that when present, disc winds from XRBs are more ionized (at a given inclination angle) than those in AGN. This might not be surprising as the discs around XRBs are expected to be more ionized than their AGN counterparts, owing to their much higher temperature. Indeed, Proga & Kallman (2002) show that the winds in LMXBs will be thermally driven from the

disc, and should in general be optically thin. Therefore, in the vast majority of cases, these outflows do not dominate the observed shape of the X-ray spectra of BHBs. The fact that the continuum of XTE J1650−500 presented here is well modelled with the standard BHB components (thermal disc at soft energies and Comptonized emission at hard energies) leads us to conclude that the X-ray spectrum of XTE J1650−500 has *not* been significantly modified by any additional complex absorption in this observation. Furthermore, in Section 3.1.6 we have demonstrated that the *XMM–Newton* data exclude the possibility that the iron line profile may have been modified by a strong, relativistic outflow similar to that proposed by Done & Gierliński (2006). We briefly note that high-mass X-ray binaries (HMXBs) also frequently display fairly strong absorption features (e.g. Cygnus X-1; see Hanke et al. 2009), but the absorption in these sources is expected to originate due to the strong stellar winds of their companions from which the BH accretes.

In contrast to the evidence for ionized outflows in LMXBs, although the profile of the excess emission evolves with inclination, its presence does not. The growing picture then is that many observations of XRBs show evidence for broad excesses at around ∼6–7 keV, despite these sources being observed at a large range of inclinations. The vast majority of these sources do not display any evidence for significant modification by complex absorption above that expected due to the ISM. These excesses cannot then be associated with the presence of disc winds, and must be intrinsic to the source.

4.2 Common origin

If these excesses are not associated with complex absorption, as we have argued is highly likely, they must arise due to some emission process. Limiting ourselves to atomic processes, as we wish to simultaneously explain the excesses seen in XRBs and AGN, the energies at which they are observed strongly suggest an association with iron emission. Previous works have provided detailed comparisons of the various processes which may broaden one or more iron emission lines into an emission feature as broad as those observed in XRBs (e.g. Hiemstra et al. 2011), and frequently conclude that, assuming the emission features are truly as broad as they appear, it is highly likely they have primarily been broadened by relativistic effects, which in turn requires the intrinsic emission to arise close to the black hole. Indeed, we have considered the main alternative for XRBs, namely that Compton broadening dominates, in some detail for the case of XTE J1650−500, and have determined that the scenario in which relativistic broadening dominates is strongly preferred (see Sections 3.1.8 and 3.1.9). We stress again that some contribution to the line width from Comptonization is unavoidable, but this is self-consistently included in the REFBHB reflection model primarily used here. Furthermore, as we are searching for a common origin for the features in XRBs and AGN, we note that historically several authors have considered the possibility that Compton broadening may be the dominant effect in producing the broad lines observed in AGN, and have concluded that such a scenario is not viable for these sources (see Fabian et al. 1995; Reynolds & Wilms 2000; Ruszkowski et al. 2000).

We must therefore consider whether the excesses may be artificially broadened in some way. It has recently been claimed that instrumental effects, such as pile-up, may contribute to the broadening (see Yamada et al. 2009; Done & Diaz Trigo 2010; Ng et al. 2010). However, detailed simulations by Miller et al. (2010a) have shown statistically that pile-up most likely has the opposite effect, and should cause a narrowing of the features. Furthermore, we note

that broad features similar to that observed here have been detected in XRBs and AGNs over a variety of luminosity states, and with a variety of different detectors, including gas-based spectrometers which do not suffer at all from pile-up. For a recent review on detections of broad emission lines, see Miller (2007). In the specific case presented here, we can be confident that the spectrum of XTE J1650−500 does not suffer from pile-up effects, as the observation was taken with *XMM–Newton* in burst mode, which is specifically designed to observe extremely bright sources. This has been confirmed through comparison of the line profiles obtained in this observation and the *BeppoSAX* observation roughly a day prior; Fig. 5 shows the two are practically identical, and the *BeppoSAX* MECS detectors are gas based and thus do not suffer from pile-up. In addition, this strongly suggests that other instrumental effects, e.g. CTI, are not significantly modifying the profile of the line, as the profile appears to be independent of detector type. Therefore, we can conclude that the width of the line has a true astrophysical origin.

All the evidence points towards the excesses in XRBs being due to relativistically broadened iron emission. We stress again that, even though complex absorption may initially appear to be a plausible explanation for these features in AGN, it is not a viable solution for XRBs. Indeed, reflection of the Comptonized emission by the accretion disc is a natural and unavoidable consequence of the presence of both physical components to the accretion flow, as long as some fraction of this emission is directed towards the disc, as is expected to be the case. Provided the disc extends in to the regions of strong gravity immediately surrounding the black hole, a widely accepted geometry for black holes with high accretion rates, the reflected emission lines will be broadened and possibly skewed by the relativistic effects inherent in such a region. The high cosmic abundance and fluorescent yield of iron indicate that its primary emission features, which are known to be between approximately 6.4 and 6.97 keV (rest frame), should be the most prominent.

The presence of both an optically thick accretion disc and some Comptonizing region which produces high-energy photons is observationally confirmed for both XRBs and AGNs (see e.g. Remillard & McClintock 2006; Done et al. 2007; Elvis 2010), therefore disc reflection does not require any additional complex emission regions over those known to be present. In addition, gravitational light bending is a natural and unavoidable consequence for emission originating in a region of strong gravity in the general relativistic model, so the proposed explanation for spectral variability and steep emissivity profiles does not require any additional physics over known gravitational effects. Therefore, we argue that both disc reflection and light bending are present in AGNs. For the case of MCG–6-30-15, further evidence in favour of the presence of disc reflection/light bending interpretation is presented by Turner et al. (2004), who undertake a detailed analysis of the data obtained with the reflection grating spectrometer aboard *XMM–Newton*, and find strong evidence for a variable continuum but very little evidence for variable absorption, as would have been expected if the spectral variability was driven by changes in the absorbers. We also note that Rossi et al. (2005) find that the relative variations of the iron line and the continuum in XTE J1650−500 favour a lightbending interpretation.

In summary, since the presence of both accretion discs and Comptonizing regions in AGNs is known, disc reflection is indeed a logical consequence, as are relativistic effects when the disc extends close to the black hole. This is the most self-consistent interpretation for the broad excesses observed at ∼6 keV. Given that this process is also observed in XRBs, for which interpretations invoking complex

absorption troughs are not viable, we conclude that the fundamental emission components observed from accreting black holes are a direct thermal component from the accretion disc (which appears in the UV for AGN), a Comptonized component extending to high energies, and a reflection-dominated component arising due to irradiation of the disc by the Comptonized emission. Any intervening absorption must necessarily act on all these intrinsic emission components. Other interpretations proposed for AGN add unnecessary complexities to the theoretical framework of accretion in strong gravity, in discord with Occam's razor.

5 CONCLUSIONS

With a simple spectral analysis, we have demonstrated that the high-quality spectra from the 2001 *XMM–Newton* observations of the stellar mass BHB XTE J1650−500 and the active galaxy MCG–6-30-15 both exhibit similar broad excesses at ∼4–7 keV. These are well modelled with relativistically broadened iron emission lines. Such features are commonly observed in both LMXBs and AGN. However, in the case of active galaxies there is still a debate over whether this feature arises through fluorescent iron emission or through complex absorption processes. In this work, we highlight the similarities of the features, herein interpreted as broad iron lines, in these two sources. By stressing that the general accretion process is mass independent, as optically thick accretion discs and Comptonizing regions are present in both classes of black hole, we argue that the simplest solution for these apparent excesses in AGN is the same as that for their lower mass analogues, Galactic X-ray binaries, where we hope to have convinced the reader that the presence of relativistic disc lines is confirmed.

REFERENCES

Arnaud K. A., 1996, in Jacoby G. H., Barnes J., eds, ASP Conf. Ser. Vol. 101, Astronomical Data Analysis Software and Systems V, Astron. Soc. Pac., San Francisco, p. 17
Ballantyne D. R., Ross R. R., Fabian A. C., 2001, MNRAS, 327, 10
Ballantyne D. R., Vaughan S., Fabian A. C., 2003a, MNRAS, 342, 239
Ballantyne D. R., Weingartner J. C., Murray N., 2003b, A&A, 409, 503
Blum J. L., Miller J. M., Fabian A. C., Miller M. C., Homan J., van der Klis M., Cackett E. M., Reis R. C., 2009, ApJ, 706, 60
Blustin A. J., Page M. J., Fuerst S. V., Branduardi-Raymont G., Ashton C. E., 2005, A&A, 431, 111
Boella G., Butler R. C., Perola G. C., Piro L., Scarsi L., Bleeker J. A. M., 1997a, A&AS, 122, 299
Boella G. et al., 1997b, A&AS, 122, 327

---

[10] http://home.gna.org/veusz/

Boirin L., Méndez M., Díaz Trigo M., Parmar A. N., Kaastra J. S., 2005, A&A, 436, 195

Bondi H., 1952, MNRAS, 112, 195

Brenneman L. W., Reynolds C. S., 2006, ApJ, 652, 1028

Brenneman L. W., Reynolds C. S., 2009, ApJ, 702, 1367

Cackett E. M. et al., 2009, ApJ, 690, 1847

Cackett E. M. et al., 2010, ApJ, 720, 205

Chiang C.-Y., Fabian A. C., 2011, MNRAS, 414, 2345

Coppi P. S., 1999, in Poutanen J., Svensson R., eds, ASP Conf. Ser. Vol. 161, High Energy Processes in Accreting Black Holes, Astron. Soc. Pac., San Francisco, p. 375

Crummy J., Fabian A. C., Gallo L., Ross R. R., 2006, MNRAS, 365, 1067

Czerny B., Zbyszewska M., Raine D. J., 1991, in Treves A., Perola G. C., Stella L., eds, Lecture Notes in Physics, Vol. 385, Iron Line Diagnostics in X-ray Sources. Springer-Verlag, Berlin, p. 226

D'Aì A. et al., 2010, A&A, 516, A36

Di Salvo T., Iaria R., Méndez M., Burderi L., Lavagetto G., Robba N. R., Stella L., van der Klis M., 2005, ApJ, 623, L121

Díaz Trigo M., Parmar A. N., Boirin L., Méndez M., Kaastra J. S., 2006, A&A, 445, 179

Díaz Trigo M., Parmar A. N., Miller J., Kuulkers E., Caballero-García M. D., 2007, A&A, 462, 657

Done C., Diaz Trigo M., 2010, MNRAS, 407, 2287

Done C., Gierliński M., 2006, MNRAS, 367, 659

Done C., Gierliński M., Kubota A., 2007, A&AR, 15, 1

Elvis M., 2010, in Peterson B., Somerville R., Storchi-Bergmann T., eds, IAU Symp. Vol. 267, Co-evolution of Central Black Holes and Galaxies. Cambridge Univ. Press, Cambridge

Fabian A. C., Ross R. R., 2010, Space Sci. Rev., 157, 167

Fabian A. C., Vaughan S., 2003, MNRAS, 340, L28

Fabian A. C., Rees M. J., Stella L., White N. E., 1989, MNRAS, 238, 729

Fabian A. C., Nandra K., Reynolds C. S., Brandt W. N., Otani C., Tanaka Y., Inoue H., Iwasawa K., 1995, MNRAS, 277, L11

Fabian A. C. et al., 2002, MNRAS, 335, L1

Fabian A. C. et al., 2009, Nat, 459, 540

Fisher K. B., Huchra J. P., Strauss M. A., Davis M., Yahil A., Schlegel D., 1995, ApJS, 100, 69

García J., Kallman T. R., 2010, ApJ, 718, 695

Gendreau K., Bautz M., Ricker G., 1993, Nuclear Instrum. Methods Phys. Res. A, 335, 318

George I. M., Fabian A. C., 1991, MNRAS, 249, 352

Gierliński M., Done C., 2004, MNRAS, 349, L7

Gierliński M., Zdziarski A. A., Poutanen J., Coppi P. S., Ebisawa K., Johnson W. N., 1999, MNRAS, 309, 496

Grant C. E., Bautz M. W., Kissel S. E., LaMarr B., 2004, in Holland A. D., ed., SPIE Conf. Ser. Vol. 5501, High-Energy Detectors in Astronomy. SPIE, Bellingham, p. 177

Haardt F., Maraschi L., 1991, ApJ, 380, L51

Hanke M., Wilms J., Nowak M. A., Pottschmidt K., Schulz N. S., Lee J. C., 2009, ApJ, 690, 330

Hiemstra B., Méndez M., Done C., Díaz Trigo M., Altamirano D., Casella P., 2011, MNRAS, 411, 137

Inoue H., Matsumoto C., 2003, PASJ, 55, 625

Jansen F. et al., 2001, A&A, 365, L1

Juett A. M., Schulz N. S., Chakrabarty D., 2004, ApJ, 612, 308

Juett A. M., Schulz N. S., Chakrabarty D., Gorczyca T. W., 2006, ApJ, 648, 1066

Kaastra J. S., de Vries C. P., Costantini E., den Herder J. W. A., 2009, A&A, 497, 291

Kalberla P. M. W., Burton W. B., Hartmann D., Arnal E. M., Bajaja E., Morras R., Pöppel W. G. L., 2005, A&A, 440, 775

King A. R., Pounds K. A., 2003, MNRAS, 345, 657

Kirsch M. G. F. et al., 2006, A&A, 453, 173

Kotani T., Ebisawa K., Dotani T., Inoue H., Nagase F., Tanaka Y., Ueda Y., 2000, ApJ, 539, 413

Laor A., 1991, ApJ, 376, 90

Lee J. C., Ogle P. M., Canizares C. R., Marshall H. L., Schulz N. S., Morales R., Fabian A. C., Iwasawa K., 2001, ApJ, 554, L13

Lee J. C., Reynolds C. S., Remillard R., Schulz N. S., Blackman E. G., Fabian A. C., 2002, ApJ, 567, 1102

Lin D., Remillard R. A., Homan J., 2010, ApJ, 719, 1350

Liu B. F., Done C., Taam R. E., 2011, ApJ, 726, 10

Lodders K., 2003, ApJ, 591, 1220

Madej O. K., Jonker P. G., Fabian A. C., Pinto C., Verbunt F., de Plaa J., 2010, MNRAS, 407, L11

Malzac J., Belmont R., 2009, MNRAS, 392, 570

Miller J. M., 2007, ARA&A, 45, 441

Miller J. M. et al., 2002, ApJ, 570, L69

Miller J. M. et al., 2004, ApJ, 601, 450

Miller J. M., Raymond J., Fabian A., Steeghs D., Homan J., Reynolds C., van der Klis M., Wijnands R., 2006, Nat, 441, 953

Miller L., Turner T. J., Reeves J. N., 2008, A&A, 483, 437

Miller J. M., Reynolds C. S., Fabian A. C., Miniutti G., Gallo L. C., 2009a, ApJ, 697, 900

Miller L., Turner T. J., Reeves J. N., 2009b, MNRAS, 399, L69

Miller J. M. et al., 2010a, ApJ, 724, 1441

Miller L., Turner T. J., Reeves J. N., Braito V., 2010b, MNRAS, 408, 1928

Miniutti G., Fabian A. C., 2004, MNRAS, 349, 1435

Miniutti G., Fabian A. C., Miller J. M., 2004, MNRAS, 351, 466

Miniutti G. et al., 2007, PASJ, 59, 315

Miniutti G., Ponti G., Greene J. E., Ho L. C., Fabian A. C., Iwasawa K., 2009, MNRAS, 394, 443

Misra R., Sutaria F. K., 1999, ApJ, 517, 661

Mitsuda K. et al., 1984, PASJ, 36, 741

Miyakawa T., Ebisawa K., Terashima Y., Tsuchihashi F., Inoue H., Zycki P., 2009, PASJ, 61, 1355

Morrison R., McCammon D., 1983, ApJ, 270, 119

Nakajima H. et al., 2008, PASJ, 60, 1

Nandra K., O'Neill P. M., George I. M., Reeves J. N., 2007, MNRAS, 382, 194

Nardini E., Fabian A. C., Reis R. C., Walton D. J., 2011, MNRAS, 410, 1251

Neilsen J., Lee J. C., 2009, Nat, 458, 481

Ng C., Díaz Trigo M., Cadolle Bel M., Migliari S., 2010, A&A, 522, A96

Orosz J. A., 2003, in van der Hucht K., Herrero A., Esteban C., eds, IAU Symp. Vol. 212, A Massive Star Odyssey: From Main Sequence to Supernova. Cambridge Univ. Press, Cambridge, p. 365

Orosz J. A., McClintock J. E., Remillard R. A., Corbel S., 2004, ApJ, 616, 376

Owen J. E., Ercolano B., Clarke C. J., Alexander R. D., 2010, MNRAS, 401, 1415

Petrucci P. O., Merloni A., Fabian A., Haardt F., Gallo E., 2001, MNRAS, 328, 501

Piconcelli E., Jimenez-Bailón E., Guainazzi M., Schartel N., Rodríguez-Pascual P. M., Santos-Lleó M., 2004, MNRAS, 351, 161

Pounds K. A., Reeves J. N., 2009, MNRAS, 397, 249

Poutanen J., Svensson R., 1996, ApJ, 470, 249

Pozdnyakov L. A., Sobol I. M., Syunyaev R. A., 1983, Astrophys. Space Phys. Rev., 2, 189

Prigozhin G. Y., Burke B. E., Bautz M. W., Kissel S. E., LaMarr B., Freytsis M., 2004, in Holland A. D., ed., SPIE Conf. Ser. Vol. 5501, High-Energy Detectors in Astronomy. SPIE, Bellingham, p. 357

Proga D., Kallman T. R., 2002, ApJ, 565, 455

Proga D., Kallman T. R., 2004, ApJ, 616, 688

Proga D., Stone J. M., Kallman T. R., 2000, ApJ, 543, 686

Reeves J. N. et al., 2006, Astron. Nachr., 327, 1079

Reeves J. N. et al., 2009, ApJ, 701, 493

Reis R. C., Fabian A. C., Ross R. R., Miniutti G., Miller J. M., Reynolds C., 2008, MNRAS, 387, 1489

Reis R. C., Fabian A. C., Ross R. R., Miller J. M., 2009a, MNRAS, 395, 1257

Reis R. C., Fabian A. C., Young A. J., 2009b, MNRAS, 399, L1

Reis R. C. et al., 2011, MNRAS, 410, 2497

Reis R. C., Fabian A. C., Miller J. M., 2010b, MNRAS, 402, 836

Remillard R. A., McClintock J. E., 2006, ARA&A, 44, 49

Reynolds C. S., Wilms J., 2000, ApJ, 533, 821

Ross R. R., Fabian A. C., 2005, MNRAS, 358, 211

Ross R. R., Fabian A. C., 2007, MNRAS, 381, 1697

Rossi S., Homan J., Miller J. M., Belloni T., 2005, MNRAS, 360, 763

Ruszkowski M., Fabian A. C., Ross R. R., Iwasawa K., 2000, MNRAS, 317, L11

Schurch N. J., Done C., Proga D., 2009, ApJ, 694, 1

Shakura N. I., Sunyaev R. A., 1973, A&A, 24, 337

Sidoli L., Parmar A. N., Oosterbroek T., Lumb D., 2002, A&A, 385, 940

Sim S. A., Proga D., Miller L., Long K. S., Turner T. J., 2010, MNRAS, 1218

Strüder L. et al., 2001, A&A, 365, L18

Sunyaev R. A., Titarchuk L. G., 1980, A&A, 86, 121

Titarchuk L., 1994, ApJ, 434, 570

Titarchuk L., Laurent P., Shaposhnikov N., 2009, ApJ, 700, 1831

Tombesi F., Cappi M., Reeves J. N., Palumbo G. G. C., Yaqoob T., Braito V., Dadina M., 2010, A&A, 521, A57

Townsley L. K., Broos P. S., Nousek J. A., Garmire G. P., 2002, Nuclear Instrum. Methods Phys. Res. A, 486, 751

Turner T. J., Miller L., 2009, A&AR, 17, 47

Turner A. K., Fabian A. C., Lee J. C., Vaughan S., 2004, MNRAS, 353, 319

Turner T. J., Miller L., Kraemer S. B., Reeves J. N., Pounds K. A., 2009, ApJ, 698, 99

Ueda Y., Murakami H., Yamaoka K., Dotani T., Ebisawa K., 2004, ApJ, 609, 325

Ueda Y., Yamaoka K., Remillard R., 2009, ApJ, 695, 888

Vaughan S., Fabian A. C., 2004, MNRAS, 348, 1415

Vaughan S., Uttley P., 2008, MNRAS, 390, 421

Vaughan S., Boller T., Fabian A. C., Ballantyne D. R., Brandt W. N., Trümper J., 2002, MNRAS, 337, 247

Vaughan S., Fabian A. C., Ballantyne D. R., De Rosa A., Piro L., Matt G., 2004, MNRAS, 351, 193

Walton D. J., Reis R. C., Fabian A. C., 2010, MNRAS, 408, 601

Wilkins D. R., Fabian A. C., 2011, MNRAS, 408

Wilkinson T., Uttley P., 2009, MNRAS, 397, 666

Wilms J., Allen A., McCray R., 2000, ApJ, 542, 914

Yamada S. et al., 2009, ApJ, 707, L109

Young A. J., Lee J. C., Fabian A. C., Reynolds C. S., Gibson R. R., Canizares C. R., 2005, ApJ, 631, 733

Zoghbi A., Fabian A. C., Uttley P., Miniutti G., Gallo L. C., Reynolds C. S., Miller J. M., Ponti G., 2010, MNRAS, 401, 2419

APPENDIX A: GAIN FITS AND BROAD LINES

Here we present simulations demonstrating the effect of applying a constant multiplicative gain shift on the results obtained mod-

elling features in the iron K energy region. We simulate data using the *EPIC*-pn response files from a simple model consisting of an absorbed power law ($N_H = 7 \times 10^{21}$ atom cm^{-2}, $\Gamma = 2.15$) and a Gaussian emission line with an EW of 350 eV at 6.4 keV. The exposure time for each simulated data set was 1000 s. We then attempt to model this data with the same components, but with a multiplicative 3 per cent gain shift applied to shift the response to lower energies (equivalent to shifting the data to higher energies by the same amount, the approach taken by EPFAST). These values were chosen to best represent the case presented in the main body of the paper. This process is repeated 1000 times, for both narrow ($\sigma = 0.0$ keV) and broad ($\sigma = 1.1$ keV) line profiles (line widths were fixed throughout the modelling process, but continuum parameters could vary). In each case, the obtained line energy was obtained, and compared with 6.4 keV. The results are displayed in Fig. A1. For narrow line profiles (left-hand panel), the line energies are tightly clustered around ∼6.6 keV (∼3 per cent difference), as expected given the applied gain shift. This is because the feature is strong and narrow, and hence changes in the underlying continuum do not significantly affect the energy obtained.

The same is not true when the broad line profile is considered (Fig. A1, right-hand panel). Even though a gain shift of 3 per cent is applied, we see that the energy obtained is systematically shifted by a much larger amount, and the line centroid obtained is typically ∼7 keV (∼9 per cent shift). This is because, unlike for a narrow line, the energy obtained for a broad line does depend somewhat on the underlying continuum model. The application of a constant multiplicative gain shift falsely increases the high-energy curvature present in the data relative to the original continuum model; data simulated with a simple power-law model display visible, concave curvature (turning up at high energies) when the response is shifted to lower energies (see Fig. A2, left-hand panel). This additional curvature conspires to further increase the energy centroid obtained for a broad line profile.

Finally, before we can relate this back to the shift in the line centroid energy observed when applying EPFAST, we must first confirm that EPFAST and the 'gain fit' command in XSPEC used in the above simulations do indeed have the same effect at high energies. To do this, we apply the basic reflection interpretation (model 1) to the unmodified *XMM–Newton* data with the 3 per cent gain shift used in the above simulations. Only the overall normalization of the
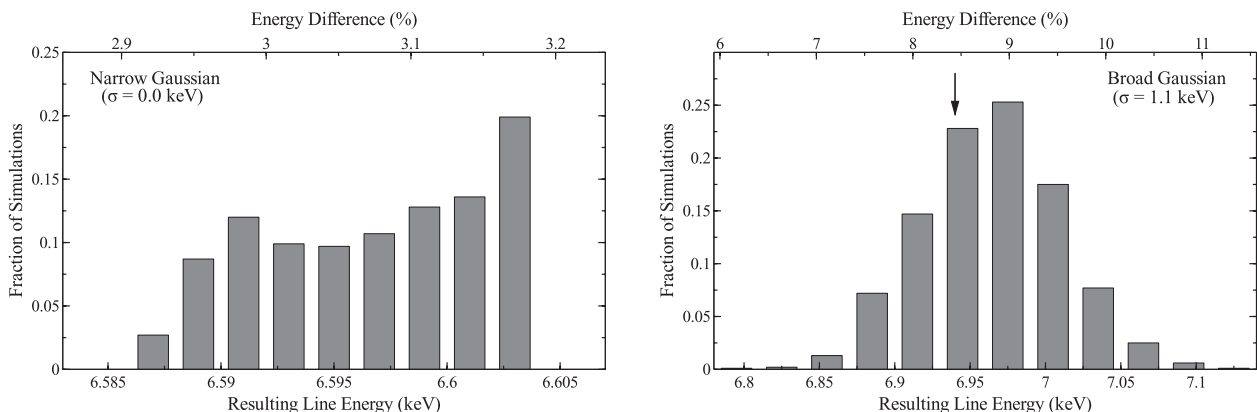
Figure A1. Distributions of the energy centroids obtained for both narrow ($\sigma = 0.0$ keV; left-hand panel) and broad ($\sigma = 1.1$ keV; right-hand panel) Gaussian line profiles from the gain fit simulations described in the text. The lines were initially simulated at 6.4 keV, and the energy centroids were measured again after the application of a 3 per cent constant multiplicative gain shift, as applied by EPFAST for the case of XTE J1650−500. The line centroids for the broad profile are systematically shifted by much more than the gain shift applied. The energy shift obtained for the broad line with the EPFAST-modified data in this work is indicated with an arrow, clearly consistent with the simulated distribution.
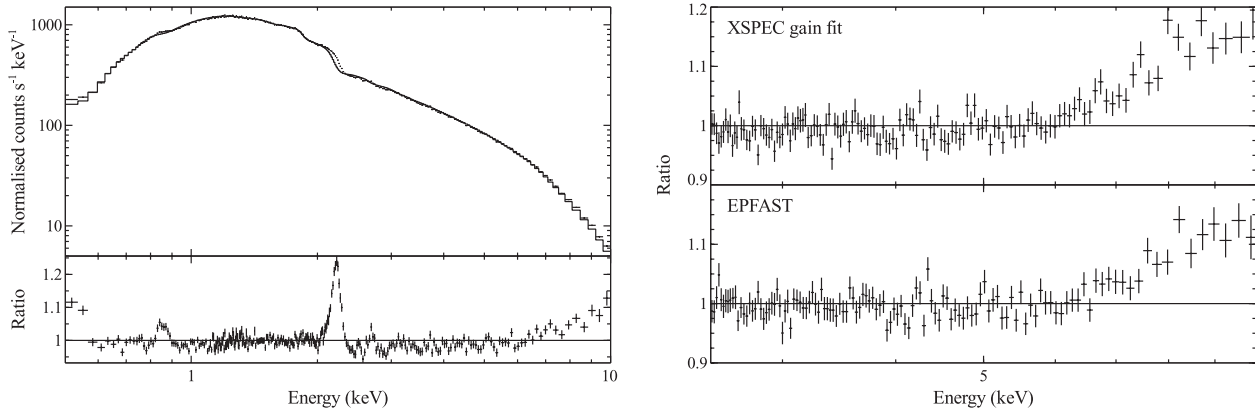
Figure A2. Left-hand panel: data simulated with an absorbed power-law model using the *XMM–Newton* responses. The same model has been fit to the data, but with a 3 per cent multiplicative gain fit applied. In addition to the expected differences at the major absorption and instrumental edges, the gain fit clearly results in additional, artificial curvature in the continuum at high energies. Right-hand panel: a comparison of the effect of applying EPFAST and the xspec 'gain fit' command (see text). The two are found to introduce identical curvature at high energies.
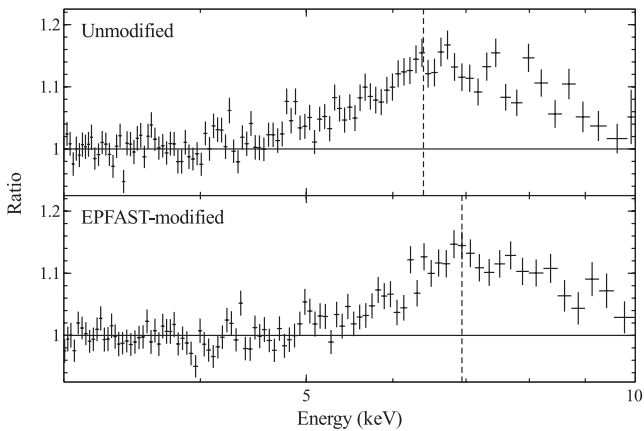
Figure A3. The unmodified (top) and EPFAST-modified (bottom) *XMM–Newton* line profiles; line energies obtained when using a Gaussian profile are shown by the dashed lines. The additional curvature at high energies introduced by EPFAST causes the centroid of the broad line profile to shift by a larger amount than the tool formally applies.

model is free to vary; all other parameters are fixed at the values in Table 3. Examining the data/model ratio (Fig. A2; right-hand panel, top), the same high-energy curvature as highlighted previously can be seen. Next we apply this model (with no gain shift) to the EPFAST-modified data, again only allowing the overall normalization to vary. Examining the data/model ratio here (Fig. A2; right-hand panel, bottom), we see identical curvature. It is clear from this comparison that the use of EPFAST has the same effect at high energies as the xspec gain fit command, also introducing additional curvature into the high-energy continuum. We therefore conclude that the shift of ~0.55 keV in the line energy obtained with the EPFAST-modified data in the main body of this paper, highlighted again in Fig. A3, has been strongly amplified by the incorrect influence of EPFAST on the continuum, and is a natural consequence of its application in this instance.

This paper has been typeset from a TEX/LATEX file prepared by the author.